



Glottis motion effects on the particle transport and deposition in a subject-specific mouth-to-trachea model: A CFPD study

Jianan Zhao^a, Yu Feng^{a,*}, Catherine A. Fromen^b

^a School of Chemical Engineering, Oklahoma State University, Stillwater, OK 74078, USA

^b Department of Chemical and Biomolecular Engineering, University of Delaware, Newark, DE 19716, USA

ARTICLE INFO

Keywords:

Glottis adduction and abduction
Generalized glottis motion function (GGMF)
Dynamic mesh
Computational fluid-particle dynamics (CFPD)

ABSTRACT

Background: Computational Fluid-Particle Dynamics (CFPD) models have been employed to predict lung aerosol dynamics for decades, estimating the delivery efficiency of inhaled drugs into the tracheobronchial tree. However, existing CFPD models assume the glottis is static during the breathing cycle. Failing to capture the dynamic motion of the glottis may introduce significant errors in drug deposition estimations.

Methods: A novel CFPD model was developed with the capability of modeling the glottis motion using the dynamic mesh method. To explore the causal relationships between the glottis motion and the inhaled drug particle dynamics, simulations were performed to compare static and different dynamic glottis models in a subject-specific mouth-to-trachea geometry under idealized sinusoidal and realistic breathing waveforms. By defining the movement of each node in the glottis region using a generalized glottis motion function (GGMF) validated with clinical data, the abduction and adduction of the glottis were accurately described. Transient transport characteristics of inhaled particle-laden airflows were investigated and analyzed, including the glottis motion effect on the inhaled particles with the aerodynamic diameters from 0.1 to 10 μm .

Results: Numerical results indicate that the static glottis assumption deviates the total deposition fraction predictions by more than 8% in relative differences. Compared with the CFPD models with the static glottis assumption, the dynamic glottis model can more realistically predict the complexity of the secondary flows near the vocal fold and the resultant particle depositions. Inter-subject variabilities of the glottis motion patterns were observed, and their influences on particle transport dynamics are not uniform. Parametric analyses also demonstrate that the maximum deformation ratio of the glottis is a key feature to describe whether the glottis motion can enhance or reduce particle depositions in the mouth-to-trachea region, over the static glottis model. **Conclusions:** The glottis motion shows a significant influence on the accuracy of predicting inhaled particle dynamics, and it should be integrated into CFPD simulations validated by subject-specific glottis motion data from clinical studies in the future. Furthermore, the proposed dynamic glottis model has been demonstrated to be a computationally effective method to recover the physiologically realistic motions of the glottis, and ready to be added into the next-generation holistic virtual lung modeling approach.

1. Introduction

According to the National Vital Statistic Report [1], Chronic Obstructive Pulmonary Disease (COPD) and other restrictive and obstructive lung diseases are global severe health problems with rising prevalence and treatment costs [1,2]. As the primary drug delivery methodology, non-invasive delivery of pharmaceutically related aerosols through inhalation is increasingly popular for the treatment of COPD, asthma, allergies, and influenza [3]. Aerosolized drug delivery will transport medications to the sites of action without reducing

bioavailability [4]. However, conventional aerosol drug delivery using uncontrolled drug particle shapes is inefficient, with a large amount of the therapeutic depositing in the mouth-to-trachea region and an overall low dosage delivered to the designated lung sites, *i.e.*, small airways. Given the fact that existing pulmonary drug delivery approaches allow a major fraction of aggressive medications to deposit on healthy tissue, it is critical to developing new inhalable targeting methods to avoid drug particle deposition from mouth to trachea. This will enable higher delivery into the tracheobronchial tree to enhance the therapeutic outcomes, eliminate undesired side effects, and reduce healthcare costs.

To improve aerosol drug delivery, accurate predictions of drug

* Corresponding author. School of Chemical Engineering, Oklahoma State University, 420 Engineering North, Stillwater, OK, 74078, USA.

E-mail address: yu.feng@okstate.edu (Y. Feng).

Nomenclature		Greek symbols	
<i>Acronyms</i>		ω	Angular Frequency
CFPD	Computational Fluid-Particle Dynamics	$\vec{\omega}$	Vorticity
COPD	Chronic Obstructive Pulmonary Disease	<i>Subscripts</i>	
DG	Dynamic Glottis	β	Index of the terms in Fourier series
DF	Deposition Fraction	c	Breathing cycle
FEA	Finite Element Analysis	g	Glottis
FSI	Fluid-Structure Interaction	p	Peak
GGMF	Generalized Glottis Motion Function	P	Particle
IDG	Idealized Dynamic Glottis	<i>Superscripts</i>	
LES	Large Eddy Simulation	BM	Brownian Motion
PM	Particulate Matter	D	Drag
RANS	Reynolds Averaged Navier-Stokes	G	Gravity
RDF	Regional Deposition Fraction	L	Lift
RDG	Realistic Dynamic Glottis	P	Particle
SG	Static Glottis	T	Turbulence
SST	Shear Stress Transport	*	Nondimensionalized Variables
TKE	Turbulence Kinetic Energy		
UDF	User-Defined Function		

particle transport and deposition in human respiratory systems are critically needed, especially in terms of how breathing patterns and drug particle sizes in tandem can influence the drug delivery efficiency to the small airways. To address the deficiencies mentioned above, researchers have been employing computational fluid-particle dynamics (CFPD) to investigate the transport phenomena of airflow and inhaled aerosols in human pulmonary routes for decades [5–10]. Compared to *in-vitro* and *in-vivo* methods, CFPD models are time-saving and cost-effective. Properly validated, they can provide high-resolution results of and new physical insight into the transport and deposition of respirable therapeutic and toxic particulate matters (PM) in human respiratory systems [11–13]. Recently, Mortazavy et al. [14] applied a CFPD model to simulate sneezing scenarios in a subject-specific upper airway model. They simulated steady-state airflows, which simplified the dynamic transient sneezing event by using constant expiratory flow rates. Yeom et al. [15] combined CFD and finite element analysis (FEA) methods to study the airflow structures in three upper airway models reconstructed normal-mild, moderate, and severe patients suffering from obstructive sleep apnea (OSA), respectively. They also applied a machine learning approach to predict airflow structures based on CFD-FEA results. Employing both using Large Eddy Simulation (LES) and Reynolds-Averaged Navier-Stokes (RANS) models, Koullapis et al. [16] predicted and compared regional aerosol depositions in human airways. Their results show that the transport and deposition predictions of ultrafine particles are sensitive to the selection of turbulence models. Other computational lung aerosol dynamics efforts longer ago are well discussed and documented in several review papers [17,18].

Early CFPD studies [19–23] have shown the significant influence of the glottis aperture on the accuracy of predicting pulmonary airflow velocity, pressure fields, and the resultant particle deposition. Despite this known significance, most existing CFPD models of the human airway assume the glottis is static during the breathing cycle and neglect the dynamic glottis abduction and adduction. This failure to incorporate the physiologically realistic motion in the mouth-to-trachea region may influence the accuracy of simulation results.

To date, limited efforts have been made to understand the glottis motion and its effect on pulmonary airflow patterns, either clinically or using CFPD simulations. According to those studies, the variation of glottis opening may significantly influence the efficacy of pulmonary drug delivery. For example, Scheinherr et al. [19,20] clinically visualized the glottis abduction and adduction associated with different breathing intensities for both male and female volunteers. They found

that the vocal fold will open more with the increase of inspiratory flow rate, while it becomes narrower with the increase of expiratory flow rate. The only numerical study with the glottis motion in existing studies was performed by Xi et al. [24], which focuses on understanding how glottis motion can influence the airflow patterns using dynamic mesh and Large Eddy Simulation (LES). Besides, the magnetic resonance imaging (MRI) technique was used by Bates et al. [25] to capture the *in vivo* motion of the mouth-to-trachea region, which potentially facilitates the optimization and validation of the CFD simulations of airway deformations. Experimentally, Kourmatzis et al. [26] investigated how the upper airway deformation can influence the drug particle deposition using a Next Generation Impactor (NGI) and deformable silicone airway cast. Experimental findings suggest that the lateral upper airway deformation does affect the particle deposition.

Still absent from literature is the systematic understanding of how glottis motion will influence inhalable therapeutic particle dynamics and targeted delivery efficiency in human respiratory systems. Therefore, the research objective of this study is to (1) capture the unique glottis motion using the dynamic mesh method with a generalized glottis motion function (GGMF), and (2) evaluate the significance of the glottis motion on the pulmonary airflow and particle transport phenomena associated with different breathing waveforms. To the best of our knowledge, this is the first time that a GGMF has ever been developed and validated with clinical data [19,20]. It is also the first research to investigate the dynamic glottis (DG) motion effect on the accuracy of inhaled therapeutic particle deposition predictions compared with the CFPD model with the static glottis (SG) assumption. In detail, two types of DG models were performed, including the idealized sinusoidal dynamic glottis (IDG) motions and the realistic dynamic glottis (RDG) motions [19,20]. Parametric analyses were done based on the CFPD simulation results using a subject-specific mouth-to-trachea model. At different breathing flow rates, significant influences were discovered between SG and DG cases in terms of airflow structures, *i.e.*, laryngeal jet and turbulence kinetic energy (TKE), as well as the characteristics of particle transport and depositions. Numerical results demonstrate the importance of physiological correctness of glottis motion associated with realistic drug particle inhalation patterns. The GGMF developed in this study not only improves the fundamental understanding of how physiologically realistic glottis motion can influence the inhaled particle dynamics but also offers a more realistic and accurate CFPD model that can benefit the optimization of subject-specific pulmonary targeted drug delivery. Such advances to CFPD based models are essential to the

development of more efficient treatments for restrictive and obstructive lung diseases, with minimized side effects due to the unnecessary drug deposition on healthy tissues.

2. Methodology

2.1. Geometry and computational mesh

A subject-specific mouth-to-trachea geometry was employed in this study [27]. More details of the subject-specific respiratory system are shown in Fig. 1 and in other publications [13,28]. The origin (0, 0, 0) is at the center of the mouth opening, which is a disk with 20 mm in diameter. The trachea was extended to avoid flow recirculations over the outlet boundary condition. In the mouth-to-throat model, the dynamic glottis region spans from $x=0.074$ m to $x=0.094$ m (see Fig. 1). The vocal fold locates at the plane $x=0.084$ m with the maximum displacement. The finite volume mesh consists of unstructured tetrahedral elements with 6 near-wall prism layers, which was generated using ANSYS Fluent Meshing (ANSYS Inc., Canonsburg, PA). The mesh independence test has been performed to determine the final mesh with the optimized balance between computational accuracy and efficiency [28]. The final mesh contains approximately 4.4 million cells and 1.3 million nodes. Six near-wall prism layers were generated and refined to guarantee the thickness of the first prism layer satisfies $y^+ < 1$, where y^+ is the dimensionless wall distance [29,30]. The maximum skewness of the final mesh elements is 0.67, with a maximum aspect ratio of 22.4.

2.2. Generalized glottis motion function (GGMF)

The dynamics of the glottis motion was modeled based on available clinical measurements [19,20]. Clinical data [19,20] has shown that the anterior-posterior length at the vocal fold remains constant. At the beginning of the simulation, *i.e.*, the start of the inspiration (see Fig. 1 at $t = t_1$), the width of the glottis is always at its neutral position. For an idealized glottis motion, the glottis expands during the first half of the inspiration cycle and reaches its maximum width at the peak inhalation flow rate. Then, it starts to contract to its neutral position during the second half of the inspiration cycle. Similarly, during the expiration cycle, the glottis contracts to its minimum width at the peak expiratory flow and expands back to its neutral position at the end of a breathing cycle. Based on the fact that the displacement of each surface mesh node

is a function of both time and space in the dynamics glottis region, a generalized function (*i.e.*, GGMF) was proposed to capture the glottis motion. The GGMF is defined as

$$y(x, t) = (d_{g,r} - 1)f(x)g(t) + y_{r,0} \quad (1)$$

$$f(x) = \sin^m \left(\frac{x - x_1}{x_2 - x_1} \pi \right) \quad (2)$$

$$g(t) = a_0 + \sum_{\beta=1}^n [a_{\beta} \cos(\beta\omega t) + b_{\beta} \sin(\beta\omega t)] \quad (3)$$

where $y_{r,0}$ is the initial y -coordinate of the surface mesh node, and $d_{g,r}$ is the deformation ratio between maximum glottis width and the glottis width at the neutral position (see Fig. 1). x_1 and x_2 are 0.074 and 0.094 m, respectively. The nodal displacement function $g(t)$ is a time-dependent Fourier series defining the nodal motion. It is worth mentioning that $g(t)$ can be simplified to a sinusoidal function to simulate the idealized glottis motion in this study (see Fig. 2 (a)). Furthermore, $f(x)$ describes the motion of the glottis region along the x -direction to achieve a smooth transition from the maximum vocal fold deformation ($x = 0.084$ m) to the zero-displacement airways ($x \leq 0.074$ m and $x \geq 0.094$ m). The positive exponent m can be optimized based on different intensities of glottis adduction and abduction. Large m indicates fast decay of the deformation ratio in x -direction from the vocal fold ($x = 0.084$ m) to $x = 0.074$ m and $x = 0.094$ m. The dynamic glottis model based on Eqs. (1)–(3) can accurately describe different glottis abduction and adduction motions. The optimization and validations with clinical data [19,20] are shown in Fig. 2 (a)–(c). Specifically, The exponent index m is equal to 4.0. An example is shown in Fig. 1, where the variations of the cross-sectional area of the vocal fold are associated with an idealized sinusoidal breathing waveform.

2.3. Computational fluid-particle dynamics (CFPD) model

2.3.1. Continuous phase

The Transition Shear-Stress Transport (SST) model [30] was employed to predict the laminar-to-turbulence transitional airflow regime in the mouth-to-trachea geometry. The accuracy of the Transition SST model has been experimentally validated by previous studies [11,13,27]. Specifically, the conservation laws that govern the pulmonary airflow transport are given as

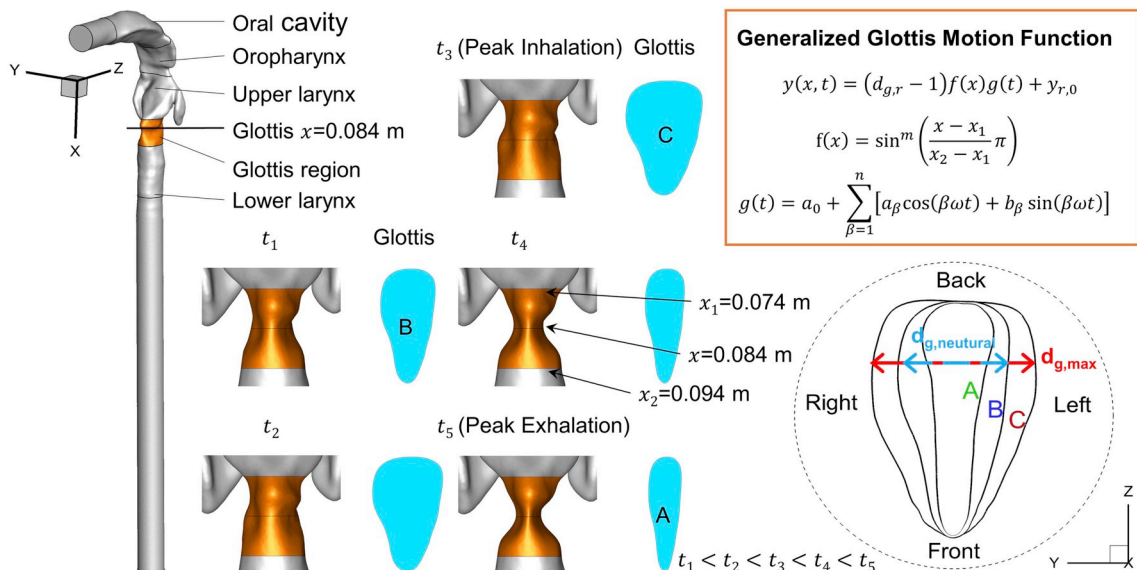


Fig. 1. The mouth-to-trachea geometry and dynamic glottis modeling framework using the generalized glottis motion function (GGMF).

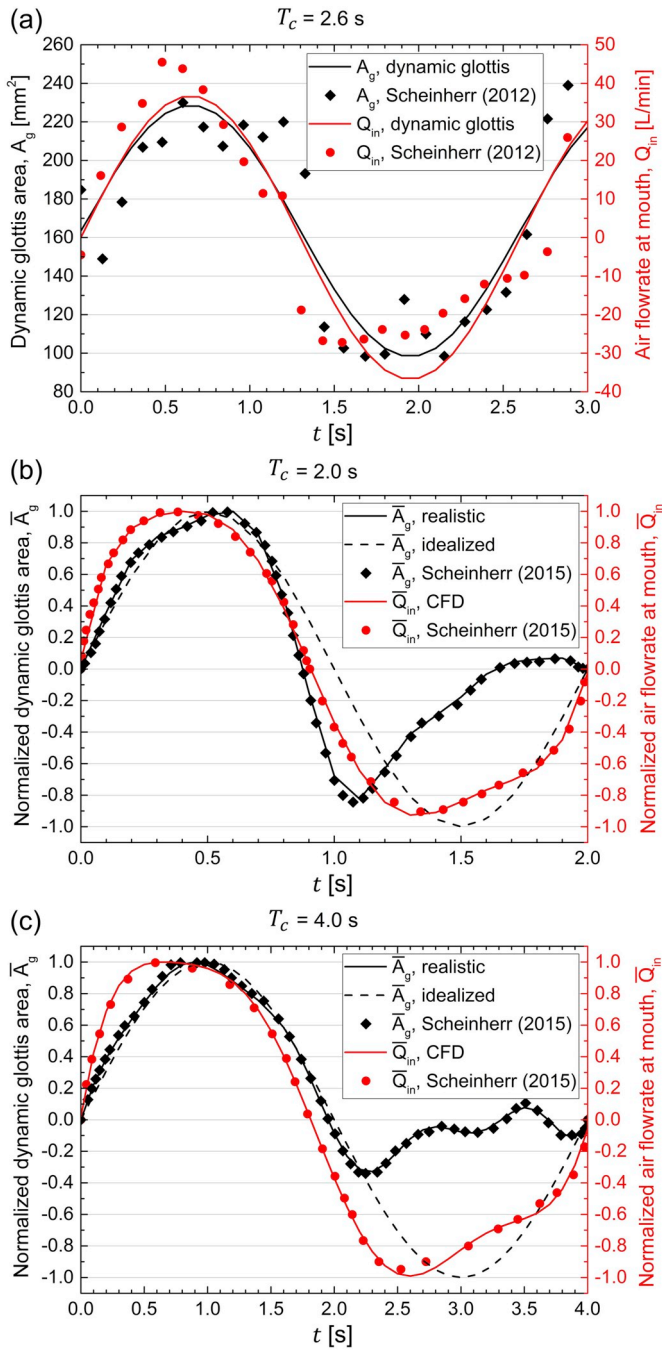


Fig. 2. Optimizations and validations of glottis motion using clinical data: (a) Idealized sinusoidal waveform; (b) Realistic 2-s breathing waveform; and (c) Realistic 4-s breathing waveform.

$$\frac{\partial u_i}{\partial x_i} = 0 \quad (4)$$

$$\rho \frac{\partial u_i}{\partial t} + \rho \frac{\partial (u_j u_i)}{\partial x_j} = -\frac{\partial p}{\partial x_i} + \frac{\partial}{\partial x_j} \left[(\mu + \mu_t) \left(\frac{\partial u_i}{\partial x_j} + \frac{\partial u_j}{\partial x_i} \right) \right] + \rho g_i \quad (5)$$

where u_i represents the averaged air velocity component in the i -direction, g_i is the gravity, p is the pressure, and μ_t is the turbulent viscosity.

2.3.2. Particulate phase

A one-way coupled Euler-Lagrange approach was employed to predict the trajectory of each particle *via* mouth inhalation [13]. Particles were assumed to be spheres with constant aerodynamic diameters

($0.1 \mu\text{m} \leq d_p \leq 10 \mu\text{m}$), and the particle density was set to 1000 kg/m^3 [31,32]. The particle volume fraction at the injection plane is less than 1%. Therefore, the particle-particle interactions are neglected. The translational motion of each particle was obtained by solving the reduced Maxey-Riley equation [33]. Specifically, to determine the particle velocity u_i^p and position x_i^p [28], the following equations were discretized and solved numerically, *i.e.*,

$$\frac{dx_i^p}{dt} = u_i^p \quad (6)$$

$$m_p \frac{d}{dt} (u_i^p) = F_i^D + F_i^L + F_i^{BM} + F_i^T + F_i^G \quad (7)$$

where m_p is the particle mass, F_i^D is the drag force [34], F_i^G is the gravitational force, F_i^{BM} is the random force induced by Brownian motion [12,35], F_i^T is the force induced by turbulence [36], and F_i^L is the Saffman lift force [37]. The particle relaxation time was estimated based on the previous work [13].

Particle depositions in the mouth-to-trachea geometry can be quantified using the regional deposition fraction (RDF) [13], which is defined by

$$\text{RDF} = \frac{\text{Number of particles deposited in a specific region}}{\text{Number of particles released at the mouth}} \quad (8)$$

2.4. Numerical setup

2.4.1. Breathing profiles and glottis motions

The idealized sinusoidal velocity profile employed in this study at the mouth opening can be given as [19]

$$v(t) = v_p \sin\left(\frac{2\pi}{T_c} t\right) \quad (9)$$

where $v_p = 2.0$ m/s is the peak inspiratory velocity magnitude and $T_c = 2.6$ s is the period of a full breathing cycle.

Two realistic breathing patterns were also employed, which were obtained from clinical measurements [20]. The transient velocity magnitude was defined by Fourier series, *i.e.*,

$$v(t) = c_0 + \sum_{\beta=1}^n [c_\beta \cos(\beta\omega t) + d_\beta \sin(\beta\omega t)] \quad (10)$$

The values of the coefficients in Eq. (10) are listed in Table 1. Fig. 2 (b) and (c) display the normalized flow rate profiles for both realistic breathing waveforms. The peak velocities are 2.57 and 3.81 m/s for cases with $T_c = 2.0$ s and $T_c = 4.0$ s, respectively.

To evaluate the glottis motion effects on airflow pattern and particle transport, both dynamic and static glottis scenarios were simulated with

Table 1

Coefficients of the truncated Fourier series describing the realistic inlet velocity profiles.

	RDG2, IDG2, and SG2	RDG4, IDG4, and SG4
ω (1/s)	0.7012	1.091
c_0 (m/s)	-15.15	-229.5
c_1 (m/s)	-10.58	61.28
d_1 (m/s)	27.58	400.1
c_2 (m/s)	21.47	249
d_2 (m/s)	14.92	-92.96
c_3 (m/s)	7.651	-67.8
d_3 (m/s)	-10.42	-87.79
c_4 (m/s)	-3.342	-12.77
d_4 (m/s)	-2.107	20.28

Table 2
 T_c and $d_{g,r}$ for different glottis motion cases (DR2, DI2, DR4, and DI4).

	RDG2	IDG2	RDG4	IDG4
T_c (s)	2.0	2.0	4.0	4.0
$d_{g,r}$	1.2	1.2	1.11	1.11

identical breathing patterns. For the sinusoidal breathing pattern [19], the dynamic glottis motion was approximated by the simplified Eq. (3), i.e.,

$$g(t) = \sin\left(\frac{2\pi}{T_c} t\right) \quad (11)$$

Both realistic and idealized dynamic glottis, as well as static glottis were studied based on the clinical data [19,20]. Fig. 2 (b) and (c) show the profiles of normalized dynamic glottis area \overline{A}_g varying with time. Specifically, the normalized dynamic glottis area \overline{A}_g is defined as

$$\overline{A}_g(t) = \frac{A_g(t) - A_g(0)}{A_{g,max} - A_g(0)} \quad (12)$$

where $A_g(0)$ is the glottis opening area of the neutral status at $t = 0$, and $A_{g,max}$ is the maximum glottis opening area. For 2.0-s and 4.0-s breathing cycles, $A_g(0)$ are 188 and 212 mm², and the maximum glottis areas $A_{g,max}$ are 224 and 236 mm², respectively. Furthermore, the peak inspiratory flow rates of the breathing waveforms shown are 72.4 L/min (see Fig. 2 (b)) and 49.3 L/min (see Fig. 2 (c)). The average inhalation flow rates for the two breathing waveforms shown in Fig. 2 (b) and (c) are 30.6 L/min and 15.3 L/min. Eight simulation cases in total were performed using different glottis motions and breathing waveforms (see Table 4). The idealized and realistic glottis motions associated with different breathing waveforms are also displayed in Fig. 2 (a)–(c) and Tables 1–3.

The time-dependent glottis motions with realistic and idealized profiles were simulated using Eqs. (3) and (11), respectively. The values of T_c and $d_{g,r}$ for each case are listed in Table 2. The coefficients in Eq. (3) are listed in Table 3. The flow time step size is 0.001 s. During the first 5 time steps of the inspiration, a total of 50,000 particles were injected through the mouth (10,000 particles at each time step) for each particle size.

2.4.2. Numerical model

The governing equations (Eq. (4)–(7)) were solved using a finite-volume based commercial program, ANSYS Fluent 2019 R1 (ANSYS Inc., Canonsburg, PA). The pressure outlet boundary condition was applied to the downstream outlet of the extended trachea. In-house user-defined functions (UDFs) were developed and compiled for (1) Simulating the real-time glottis abduction and adduction motion, (2) Specifying transient inhalation and exhalation profiles at the mouth front, (3) Recovering the anisotropic corrections on turbulence fluctuation velocities [38], (4) Modeling the Brownian motion induced forces on particles [13,39], and (5) Post-processing particle transport and deposition in the mouth-to-trachea region. Numerical simulations were performed on a local Dell Precision T7810 workstation (Intel® Xeon® Processor E5-2643 v4 with dual processors, 64 cores and 128 GB RAM) and a local Dell Precision T7910 workstation (Intel®Xeon® Processor E5-2683 v4 with dual processors, 64 cores, and 256 GB RAM). Using 32 cores, the dynamic glottis simulation with the 2.6-s breathing waveform (see Fig. 2 (a)) took approximately 108 h (4.5 days), while the static glottis simulation with the same breathing waveform took approximately 96 h (4 days).

Table 3
Coefficients of truncated Fourier series representing the two realistic glottis motions.

	RDG2	RDG4
ω (1/s)	1.038	2.832
a_0 (m)	0.7964	0.13176
a_1 (m)	0.422	0.3656
b_1 (m)	−0.933	0.4842
a_2 (m)	−1.266	−0.4406
b_2 (m)	−0.1089	0.06397
a_3 (m)	−0.7989	0.06537
b_3 (m)	0.8309	−0.02685
a_4 (m)	0.4348	−0.07851
b_4 (m)	0.6539	0.1011
a_5 (m)	0.4175	−0.02104
b_5 (m)	−0.05068	−0.02134
a_6 (m)	−0.005777	−0.02258
b_6 (m)	−0.2028	0.01957

3. Results

3.1. Model validations

As shown in Fig. 2 (a)–(c), The GGMF (see Eq. (1)) was validated by comparing the glottis openings predicted in the numerical simulations with available clinical measurements [19,20]. Good agreements can be observed between numerical results and clinical data shown in Fig. 2 (a)–(c), the validated dynamic glottis model also provides insight into the physiology of glottis motion. Specifically, the glottis expands during the first half of the inhalation and reaches its maximum width at the peak inspiratory flow rate. During the exhalation, the glottis contracts to its minimum width at the peak expiratory flow rate and expands back to its neutral position at the end of a breathing cycle. With the validations for both idealized and realistic glottis motions displayed in Fig. 2 (a)–(c), it can be concluded that the dynamic glottis model with the GGMF is accurate and can be employed to investigate the effects of subject-specific glottis motion on the transient pulmonary airflow field and the resultant particle transport and deposition in the mouth-to-trachea geometry.

3.2. Airflow field

3.2.1. Airflow velocity and pressure

Fig. 3 compares the velocity magnitude contours at the vocal fold ($x = 0.084$ m) and the sagittal plane between the IDG2.6 and SG2.6 cases. Compared with the SG2.6 case, the vocal fold abduction during the inhalation in the IDG2.6 generates more uneven velocity distributions at the glottis region, leading to a stronger jet core (see the velocity contours at the sagittal plane at $t = 0.65$ s and $t = 0.8$ s). In addition, the glottis adduction motion during the exhalation induces higher averaged velocity at the vocal fold (see Fig. 4 (b) and (c)), and intensifies the expiratory jet core (see the contours at $t = 1.6$ s to $t = 1.95$ s in Fig. 3) compared with the SG2.6 case. Thus, the glottis motion has noticeable impacts on the accuracy of transient airflow structure predictions and should be considered in CFPD models. Fig. 4 (a)–(c) display the area-averaged velocity magnitude $\|\overline{\vec{v}}\|$ and pressure \overline{p} at multiple cross-sections along the centerlines of the mouth-to-trachea geometry starting from the mouth front (l_1^* to l_6^* in Fig. 4 (a)) at the peak inspiration

Table 4
Simulation cases associated with different glottis motion types and breathing waveforms.

Case number	Abbreviation	Glottis motion type	d_{gr}	Breathing cycle period (s)	Breathing waveforms	Averaged inhalation flow rate (L/min)
Case 1	IDG2.6	Idealized	1.40	2.6	Idealized (Fig. 2 (a))	23.6
Case 2	SG2.6	Static	1.00	2.6	Idealized (Fig. 2 (a))	23.6
Case 3	RDG2	Realistic	1.11	2	Realistic (Fig. 2 (b))	30.6
Case 4	IDG2	Idealized	1.11	2	Realistic (Fig. 2 (b))	30.6
Case 5	SG2	Static	1.00	2	Realistic (Fig. 2 (b))	30.6
Case 6	RDG4	Realistic	1.20	4	Realistic (Fig. 2 (c))	15.3
Case 7	IDG4	Idealized	1.20	4	Realistic (Fig. 2 (c))	15.3
Case 8	SG4	Static	1.00	4	Realistic (Fig. 2 (c))	15.3

flow rate ($t=1/4T_c$). The nondimensionalized length l^* is defined as the ratio between the distance from the geometric center of the mouth front to the face center of the cross-section along curve AB shown in Fig. 4 (a), and the total length of curve AB. As shown in Fig. 4 (b), the $\|\bar{v}\|$ ratio between the peak inspiration and the peak expiration are different in IDG2.6 and SG2.6, i.e., 0.83 and 1.66, respectively. Comparing the vocal areas between SG2.6 and IDG2.6 at peak inspiratory and expiratory flow rates, the ratios are 0.72 and 1.66, respectively. The higher $\|\bar{v}\|$ in IDG2.6 than SG2.6 is mainly due to glottis opening changes. The secondary flow plays an insignificant role (see Fig. 3 at $t=1.95$ s). However, at peak inspiratory flow rate, it can be observed that the glottis expansion leads to stronger secondary flows and enhances the $\|\bar{v}\|$ at the vocal fold. In other words, compared with SG2.6, the stronger secondary flow and vortices generated in IDG2.6 (see Fig. 3 at $t=0.65$ s) reduce the differences of $\|\bar{v}\|$ between the two cases. Besides, Fig. 4 (c) indicates that the effect of glottis motion on $\|\bar{v}\|$ is significant in the larynx.

Similar to Fig. 4 (b), the nondimensionalized area-averaged velocity magnitude $\|\bar{v}\|$ at different mouth-to-trachea locations and times were compared among RDG2, IDG2, SG2, RDG4, IDG4, and SG4 (Cases 3 to 8) and displayed in Fig. 4 (d) and (e). The numbers at the end of those case names are the total time duration for one inhalation-exhalation cycle in

seconds. In Fig. 4 (d) and (e), $\|\bar{v}\|$ is normalized regarding $\|\bar{v}\|$ of the mouth opening at $t=1/4T_c$. The normalized time t^* is defined as $t^*=t/T_c$. Similar patterns can be found in Fig. 4 (b) and (d) that all static glottis modeling cases predict higher $\|\bar{v}\|$ or $\|\bar{v}\|$ during the inhalation compared with the dynamic glottis cases. During the exhalation, higher $\|\bar{v}\|$ profile can be observed in IDG cases compared with RDG and SG cases due to the higher adducting deformation of the glottis (also see Fig. 2 (b) and (c)).

Fig. 5 elucidates the impacts of different dynamic glottis motions and breathing waveforms on $\|\bar{v}\|$ distributions at the vocal fold and the sagittal plane. In general, the airflow field is significantly influenced by the breathing waveform and glottis motion pattern ($T_c=2.0$ s vs. $T_c=4.0$ s) at same t^* values. Comparing secondary flows at the vocal fold during the inhalation (see Fig. 5), no noticeable vortex structure is formed in RDG2, IDG2, or SG2 at $t=1/4T_c$, while apparent vortex structures are generated in RDG4, IDG4, and SG4. Although sharing the same breathing waveforms and the $\|\bar{v}\|$ distributions are similar, the vortex structures at the vocal folds are highly different between RDG4 and IDG4 (see the dash circles in Fig. 5), which indicates that simplifying the subject-specific glottis motion to the idealized sinusoidal glottis motion may cause unrealistic airflow structures and the resultant particle deposition. Specifically, only one vortex at the anterior of the vocal

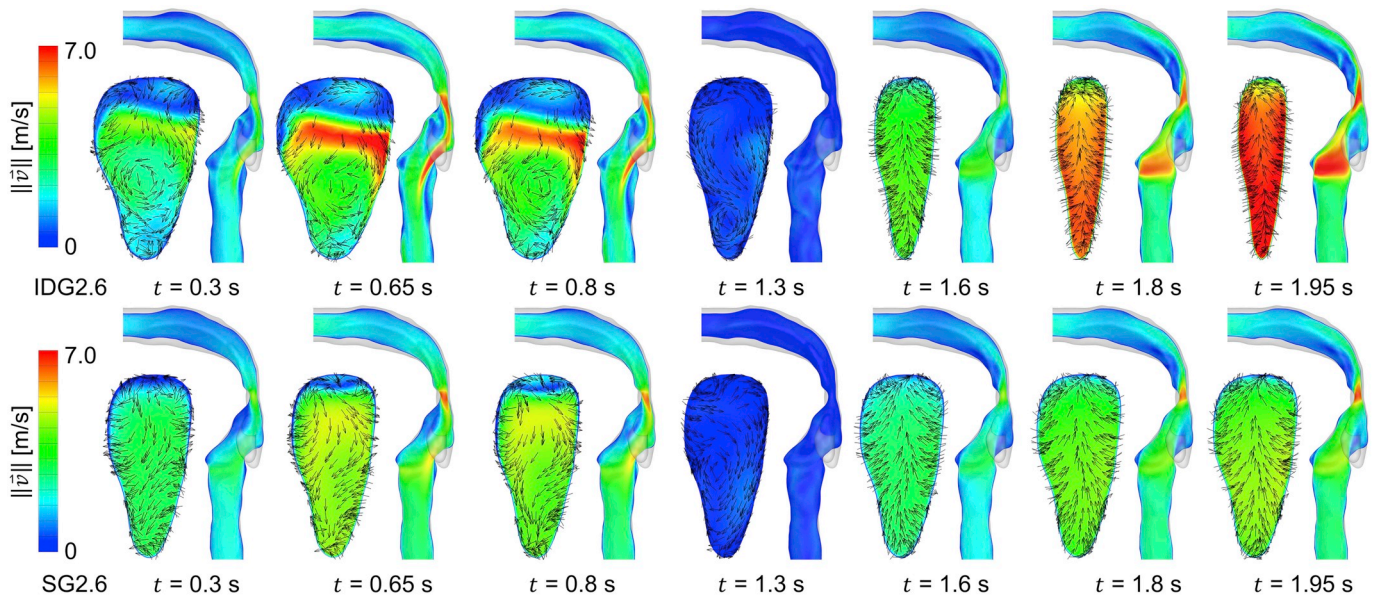


Fig. 3. Velocity magnitude contour comparisons between the idealized dynamic glottis (IDG2.6) model (top) and the static glottis (SG2.6) model (bottom) with the sinusoidal breathing waveform shown in Fig. 2 (a).

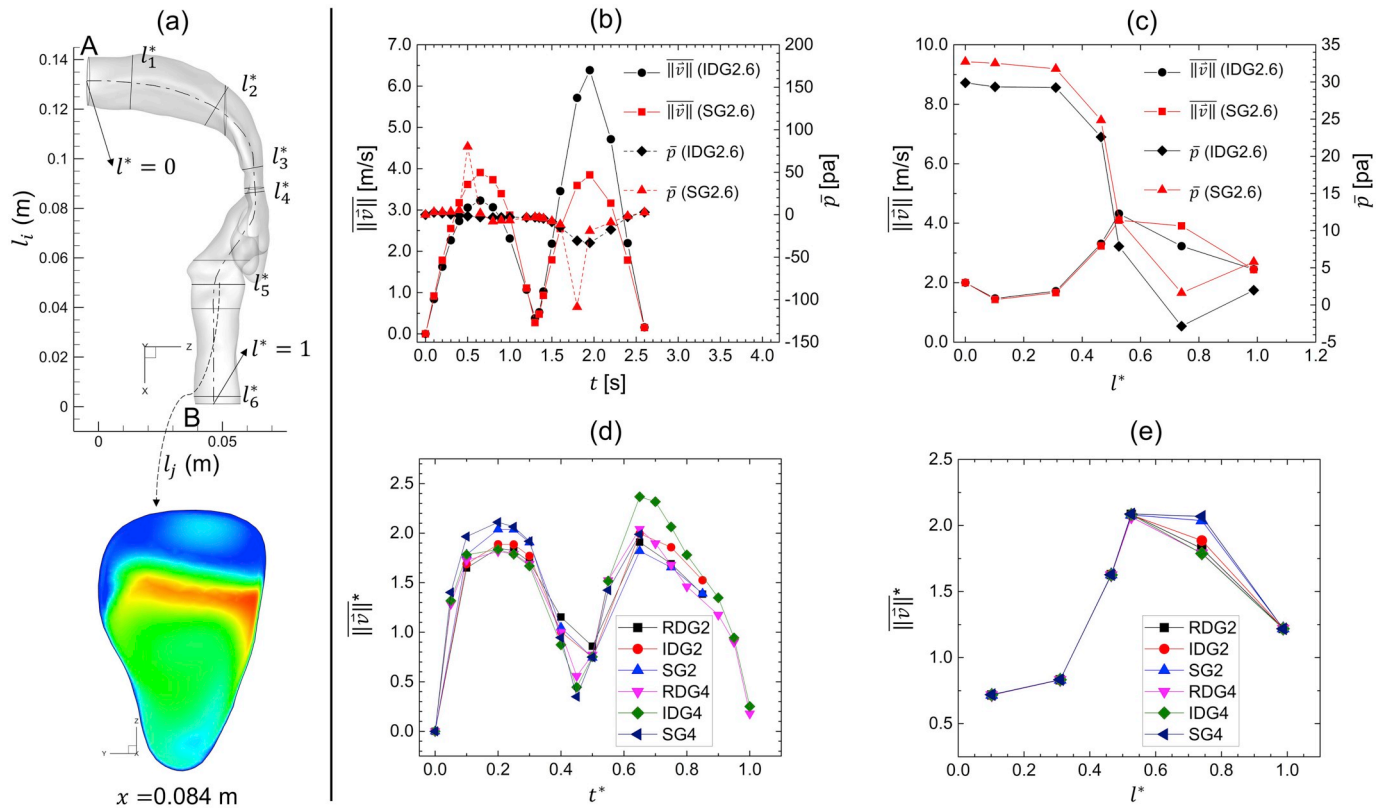


Fig. 4. Comparison of flow field parameters in the mouth-to-trachea geometry using different glottis models: (a) l_k^* locations in the mouth-to-trachea geometry, (b) area-averaged velocity and pressure at the vocal fold ($x = 0.084 \text{ m}$ or l_5^*), (c) area-averaged velocity and pressure at different cross-sections (at peak inspiration flow rate $t = 0.65 \text{ s}$), (d) the evolution of $\|\bar{v}\|$ at the vocal fold (l_5^*), and (e) $\|\bar{v}\|$ at cross-sections l_1^* to l_6^*

fold was generated in RDG4, with another vortex at vocal fold center (see the red dash circle in Fig. 5 (d)). Instead of one vortex, the IDG4 case generated two vortices (see the red dash circle in Fig. 5 (e)). During the exhalation stage ($t = 3/4T_c$), IDG4 has the highest $\|\bar{v}\|$ at the vocal fold because of the strongest glottis adduction compared with other cases (see contours at $t = 3/4T_c$ in Fig. 5).

3.2.2. Turbulence kinetic energy (TKE) and vorticity

As shown in Figs. 6–8, both glottis abduction and adduction lead to stronger turbulence and recirculations compared with the SG cases. Specifically, Fig. 6 (a)–(d) compare TKE and vorticity magnitude $\|\bar{\omega}\|$ at the vocal fold ($x = 0.084 \text{ m}$) and the sagittal plane between IDG2.6 and SG2.6 at different times. With the peak inspiratory flow rate at $t = 0.65 \text{ s}$, the glottis abduction in IDG2.6 induces higher TKE than SG2.6, with the highest TKE region located at the posterior of the vocal fold and the narrowest region at the oropharynx (see Fig. 6 (a) and (b) from $t = 0.3 \text{ s}$ to 0.8 s). At $t = 1.95 \text{ s}$ when the peak expiratory flow rate occurs, the glottis adduction also leads to higher TKEs at both the anterior and posterior of the glottis compared with SG2.6 (see Fig. 6 (a) and (b)). Fig. 6 (c) and (d) show that the vorticity magnitude $\|\bar{\omega}\|$ of the airflow in the oropharynx develops faster and is more evenly distributed with dynamic glottis motion compared with the static glottis. The comparisons displayed in Fig. 7 (a) and (b) also support the observations mentioned above. Specifically, Fig. 7 (a) shows the strengthened laryngeal jet core and the more skewed velocity distributions caused by the glottis motion. At the vocal fold shown in Fig. 7 (b), the area-averaged TKE (\overline{TKE}) in IDG2.6 is six times of the TKE in SG2.6.

The temporal evolutions of \overline{TKE} and $\|\bar{\omega}\|$ at the vocal fold are also shown in Fig. 7 (a)–(f). These results suggest that the glottis motion has a significant influence on the wake of turbulence during the inhalation.

Because of the high deformation ratio ($d_{g,r} = 1.40$) of the glottis abduction in IDG2.6, the waked turbulence has the maximum \overline{TKE} at $t = 0.7 \text{ s}$, which is higher and earlier compared with SG2.6 (see Fig. 7 (a) and (b)). In contrast, the glottis adduction has no significant impact on \overline{TKE} at the vocal fold. Fig. 6 (c) and (d) indicate more evenly distributed $\|\bar{\omega}\|$ in IDG2.6 than SG2.6. In addition, Fig. 7 (a) and (b) show that with the glottis expanding, $\|\bar{\omega}\|$ at the vocal fold in IDG2.6 is slightly higher than that in SG2.6. However, the temporal evolution of $\|\bar{\omega}\|$ at the vocal fold are similar for both cases during the inhalation (see Fig. 7 (a) and (b)). After the vocal fold reaches its maximum opening, $\|\bar{\omega}\|$ in IDG2.6 starts to decrease with the glottis adduction. Interestingly, $\|\bar{\omega}\|$ in SG2.6 continues increasing to its maximum value at $t = 0.9 \text{ s}$. During the exhalation, $\|\bar{\omega}\|$ in IDG2.6 is much higher than that in SG2.6. Fig. 7 (b) compares the differences in \overline{TKE} and $\|\bar{\omega}\|$ between IDG2.6 and SG2.6 at multiple cross-sections (i.e., l_1^* to l_6^* shown in Fig. 4 (a)) along the streamline in the mouth-to-trachea region at the peak inhalation flow rate. \overline{TKE} comparisons shown in Fig. 7 (b) indicate that the glottis abduction has an impact on \overline{TKE} in the upper region of the oropharynx, but the influence in the oral cavity is not apparent. The comparison of $\|\bar{\omega}\|$ shown in Fig. 7 (b) reveals a similar trend. Specifically, the maximum of $\|\bar{\omega}\|$ locates in the oropharynx. Furthermore, $\|\bar{\omega}\|$ in IDG2.6 is lower than SG2.6 at $t = 1/4T_c$. The possible reason is that the near-wall vorticity magnitude $\|\bar{\omega}\|$ in SG2.6 is much higher than IDG2.6, which leads to higher $\|\bar{\omega}\|$. Accordingly, the glottal motion-induced changes in the airflow pattern and vorticity can influence the particle transport in the mouth-to-trachea region.

Fig. 7 (c) shows the temporal evolutions of the nondimensionalized

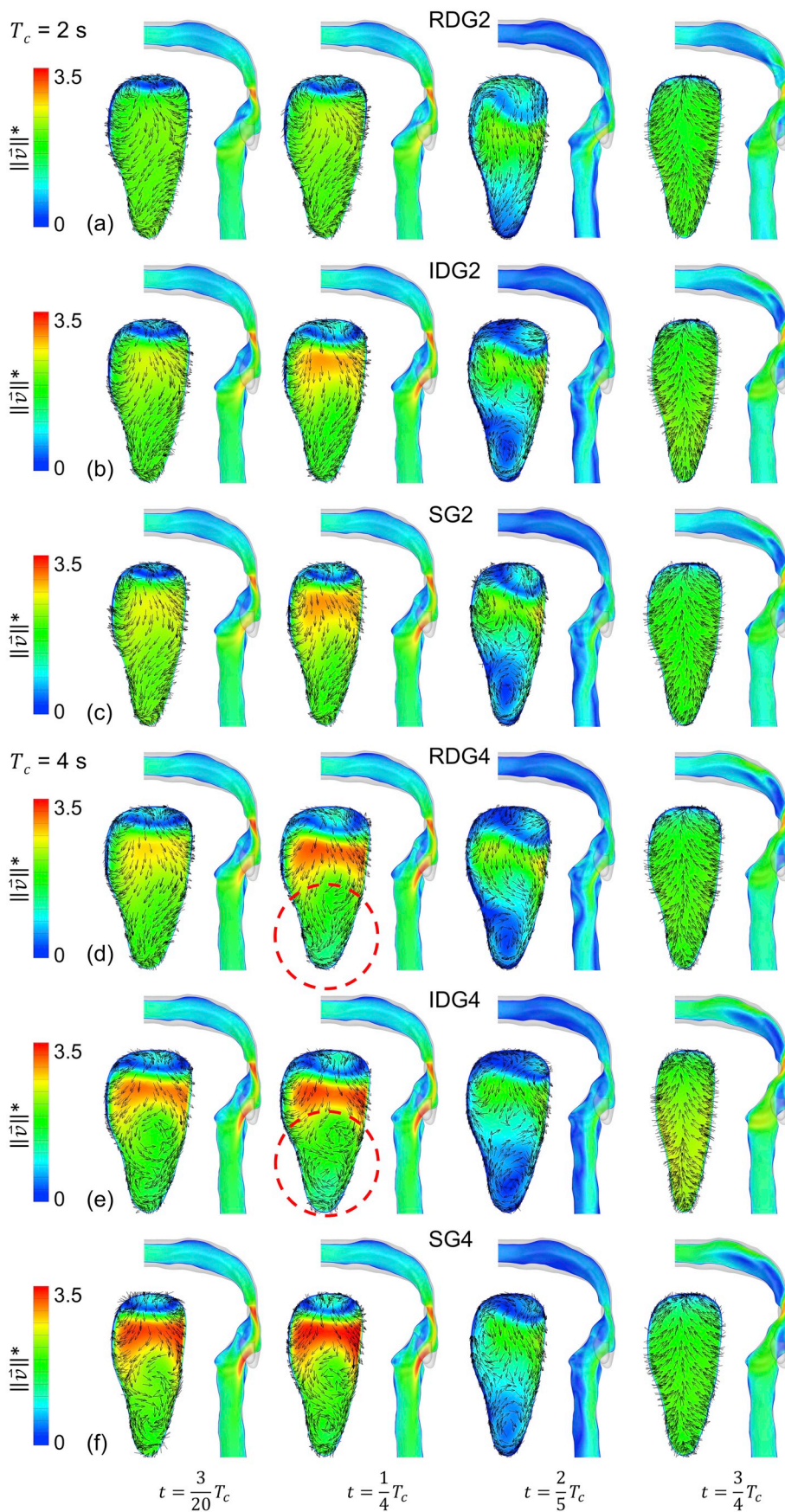


Fig. 5. Contours of nondimensionalized velocity magnitudes at the vocal fold ($x=0.084\text{m}$) and the sagittal plane with different glottis motions and breathing waveforms: (a) RDG2, (b) IDG2, (c) SG2, (d) RDG4, (e) IDG4, and (f) SG4.

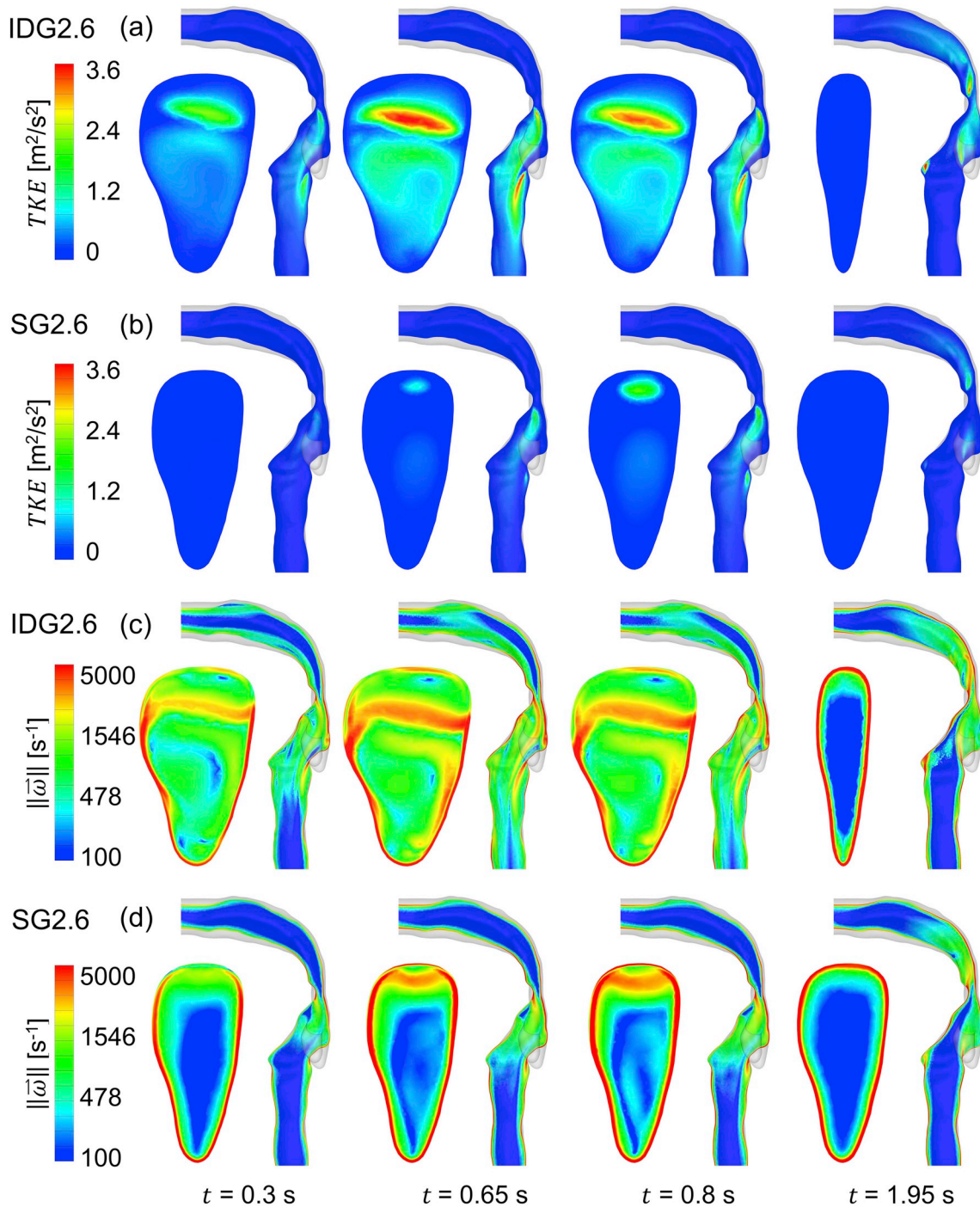


Fig. 6. Comparisons of the turbulence kinetic energy (TKE) and the vorticity magnitude $\|\vec{\omega}\|$ at the vocal fold ($x = 0.084$ m) and the sagittal plane between cases IDG2.6 and SG2.6 at different time stations: (a) TKE for IDG2.6 (b) TKE for SG2.6 (c) $\|\vec{\omega}\|$ for IDG2.6 (d) $\|\vec{\omega}\|$ for SG2.6.

turbulence kinetic energy \overline{TKE}^* at the vocal fold in RDG2, IDG2, SG2, RDG4, IDG4, and SG4 (Cases 3 to 8). Specifically, \overline{TKE}^* is defined as the ratio between the \overline{TKE} of a certain cross-section and the \overline{TKE} of the mouth front at $t = 1/4T_c$. Fig. 7 (d) displays the \overline{TKE}^* values of the cross-sections \bar{l}_1^* to \bar{l}_6^* at $t = 1/4T_c$. It can be seen from both plots that the unrealistic SG assumption can overpredict \overline{TKE}^* at the vocal fold during the inhalation, compared with the RDG and IDG cases. The comparisons of $\|\vec{\omega}\|$ among different Cases (see Table 4) are shown in Fig. 7 (e) and (f), in which $\|\vec{\omega}\|$ is defined as the ratio between the $\|\vec{\omega}\|$ of a certain cross-

section and the $\|\vec{\omega}\|$ of the mouth front at $t = 1/4T_c$. Fig. 7 (e) shows that the SG assumption also overpredicts the $\|\vec{\omega}\|$ at the vocal fold compared with the DG cases during the inhalation. Besides, IDG4 has higher $\|\vec{\omega}\|$ during the exhalation compared with RDG4, which is due to the unrealistic higher constriction ratio of the vocal fold in IDG4 than RDG4 (see Fig. 2 (c)).

Fig. 8 (a)–(d) compare \overline{TKE}^* and $\|\vec{\omega}\|$ contours at the vocal fold ($x = 0.084$ m) and the sagittal plane with different DG models at $t = 1/4T_c$. High \overline{TKE}^* values start from the posterior of the glottis and extend downstream into the epiglottis. The results shown in Fig. 8 (a)–(b)

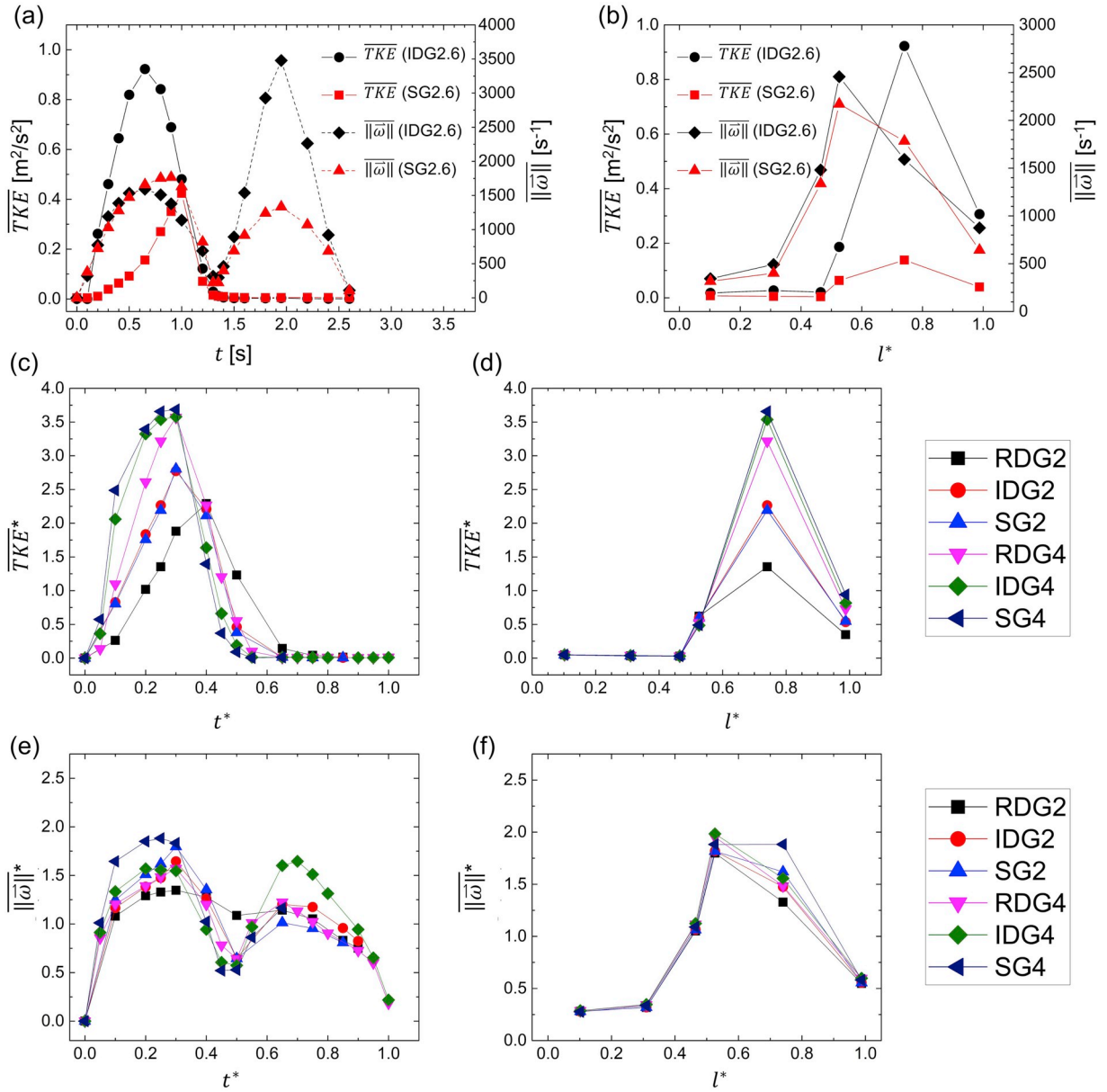


Fig. 7. Comparisons of area-averaged turbulence parameters in the mouth-to-trachea geometry using different glottis models: (a) The area-averaged TKE (\overline{TKE}) and vorticity magnitude ($\|\overline{\omega}\|$), (b) \overline{TKE} and $\|\overline{\omega}\|$ of different cross-sections at $t = 1/4T_c$, (c) time course of nondimensionalized TKE^* (\overline{TKE}^*) at the vocal fold, (d) TKE^* on l_1^* to l_6^* at $t = 1/4T_c$, (e) time course of nondimensionalized $\|\overline{\omega}\|$ ($\|\overline{\omega}\|^*$) at the vocal fold and, (f) $\|\overline{\omega}\|^*$ on l_1^* to l_6^* at $t = 1/4T_c$.

indicate that RDG2 generates the lowest TKE^* in the oropharynx. The distributions of \overline{TKE}^* at the sagittal plane also shows the faster dissipation in RDG2 at the glottis region compared with IDG2 and SG2. Such an observation can explain the relatively low profile of \overline{TKE}^* shown in Fig. 7 (c) and (d) in RDG2. The deformation ratio $d_{g,r}$ also plays a vital and complex role in altering the turbulence in the glottis region. Specifically, the glottis abduction with low $d_{g,r}$ weakens the turbulence fluctuation velocities in the glottis region, which is the reason why TKE^* is lower in RDG2 than SG2. The difference between RDG2 and IDG2 in \overline{TKE}^* distribution can be also the result of different $d_{g,r}$. Specifically in IDG2, $d_{g,r}$ is equal to zero at $t = 1/4T_c$, while $d_{g,r}$ is greater than zero in RDG2 at the same time. Such a difference demonstrates that the glottis is still expanding in RDG2 at $t = 1/4T_c$, which is the reason that the attenuation effect in RDG2 is stronger than IDG2. Additionally, as shown in Fig. 8 (b), the secondary flow (see Fig. 5 (d)–(f)) has dominant effects on the TKE^* distributions at the vocal fold. The contradictory

observations from Fig. 8 (a) and (b) compared with Fig. 6 (a) and (b) is because of the different $d_{g,r}$ values. Specifically, high $d_{g,r}$ in IDG2.6 leads to higher turbulence fluctuation velocity at the glottis region and higher TKE , while the attenuation effects become dominant with low $d_{g,r}$.

Fig. 8 (c) and (d) display $\|\overline{\omega}\|^*$ distributions among the six cases with different glottis motions and breathing waveforms (see Table 4). Specifically, the glottis abduction during the inhalation attenuates the vorticity formation in the glottis region as shown in Fig. 8 (c), which is consistent with the observations from Fig. 7 (f). With the glottis adduction motion during the exhalation, high $\|\overline{\omega}\|^*$ were formed in the oropharynx and hypopharynx. Furthermore, higher $\|\overline{\omega}\|^*$ can be observed in IDG4 and SG4 than RDG4 at the locations downstream to the vocal fold (see Fig. 8 (d)). Overall, these results indicate that the glottis motion effects on the TKE distribution at the glottis region are complex and dependent on $d_{g,r}$. With large $d_{g,r}$, the glottis abduction enhances the turbulence fluctuation velocity significantly, while the weakening effect

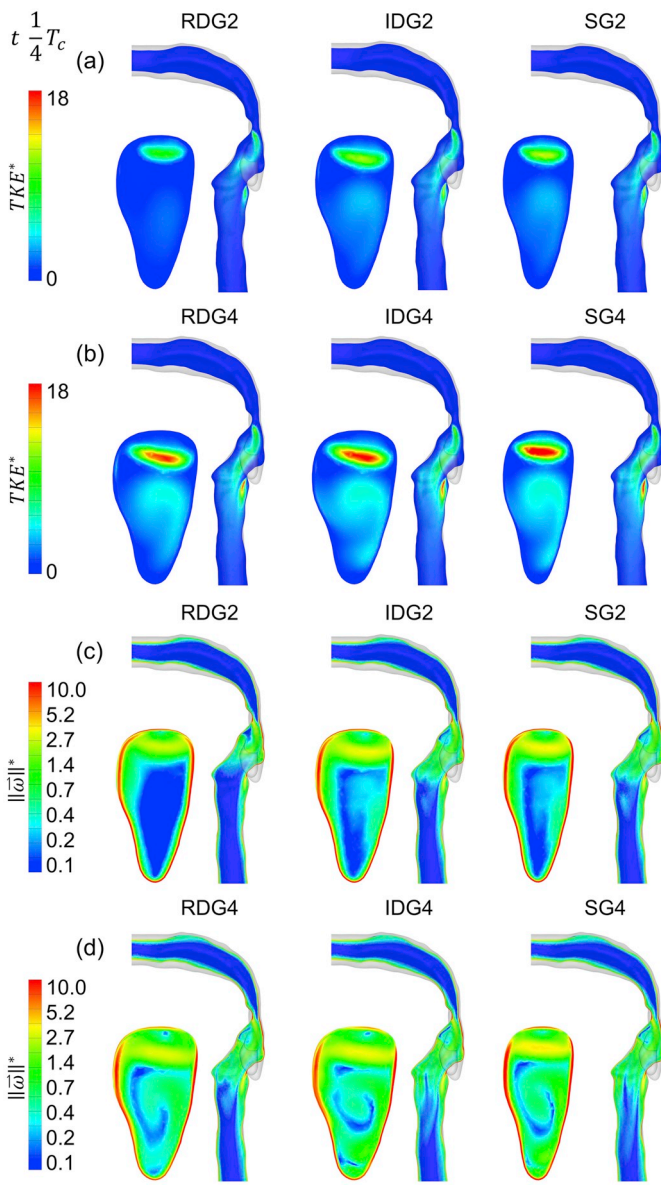


Fig. 8. Comparisons of TKE^* and $\|\vec{\omega}\|^*$ at the vocal fold ($x=0.084\text{ m}$) and the sagittal plane with different glottis motions at $t=1/4T_c$: (a) TKE^* contours of RDG2, IDG2, and SG2, (b) TKE^* contours of RDG4, IDG4, and SG4, (c) $\|\vec{\omega}\|^*$ contours of RDG2, IDG2, and SG2, and (d) $\|\vec{\omega}\|^*$ contours of RDG4, IDG4, SG4.

on the secondary flow at the glottis region is minor. On the other hand, when $d_{g,r}$ is low, the attenuation effects of the glottis abduction on turbulent velocity and secondary flow become dominant, compared with the simplified static glottis modeling results.

3.3. Particle dynamics

3.3.1. Localized particle transport and deposition patterns

To investigate the significance of the glottis motion effect on the transport and deposition of particles with different aerodynamic diameters, the transient distributions of both suspending and deposited particles are visualized in Figs. 9 and 10.

Fig. 9 shows the distributions of suspending particles in the mouth-to-trachea geometry between IDG2.6 and SG2.6 at different times. Particles are colored based on their instantaneous velocities. During the inhalation stage, particles in the larynx and glottis region have higher velocity in the static glottis case (SG2.6) than the idealized dynamic

glottis case (IDG2.6), which is because of the lower average airflow velocity induced by the glottis abduction (see Fig. 4 (b)). The glottis abduction leads to a more evenly distributed $0.1\text{-}\mu\text{m}$ particle suspensions in the upper larynx at $t=0.4\text{ s}$ than the static glottis (SG2.6). The difference is due to the larger recirculation zone formed at the anterior of epiglottis caused by the glottis abduction (see Fig. 3). For particles larger than $1\text{ }\mu\text{m}$, the particle suspending distributions are similar between IDG2.6 and SG2.6 (see Fig. 9 (c)–(h)). Furthermore, for larger particles ($d_p=5\text{--}10\text{ }\mu\text{m}$), the suspending particle cloud is more concentrated (see the red circles in Fig. 9 (e)–(h) at $t=0.3\text{ s}$), compared with the more scattered distributions of small particles ($d_p=0.1\text{ }\mu\text{m}$) shown in Fig. 10 (a) and (b).

Fig. 10 (a)–(c) show the local particle deposition patterns at the end of one inhalation-exhalation breathing cycle, colored with either the particle residence time t or normalized particle residence time t^* . As shown in Fig. 10 (a) and (b), the glottis motion incorporated in IDG2.6 results in a distinguished particle deposition pattern of submicron particles ($d_p=0.1\text{ }\mu\text{m}$) in the mouth-to-trachea region compared with SG2.6. Specifically, the $0.1\text{-}\mu\text{m}$ particle deposition in IDG2.6 concentrates in the oral cavity and pharynx (see Fig. 10 (a)), which is less evenly distributed compared with SG2.6 (see Fig. 10 (b)). With the increase in particle size, the difference of particle deposition pattern becomes less significant between IDG2.6 and SG2.6 (see Fig. 10 (a) and (b)), indicating the weakened influence of glottis motion on particle deposition. Fig. 10 (c) compares the local depositions of $1\text{-}\mu\text{m}$ particles with different glottis motions and breathing waveforms. Specifically in RDG2 and RDG4, fewer particles deposit in the lower larynx because of the attenuation effect of the glottis abduction on the localized secondary flows, which leads to the reduced interception effect on particle deposition. For all cases shown in Fig. 10 (c), the common “hot-spots” of particle depositions are (1) the oral cavity, (2) the constriction region of the epiglottis in the oropharynx, and (3) the anterior of the glottis. The high-concentration deposition at the anterior of the glottis is due to the wall contraction, as well as the enhanced recirculation and vortices in this region induced by the glottis adduction (see Fig. 5). Indeed, the glottis adduction and the waked secondary airflows increase the chance for the particles to deposit when penetrating the vocal fold. In conclusion, the glottis motion can affect the transport of small particles in the larynx and glottis region because of their higher vulnerability to be influenced by the secondary flows compared to larger particles. The glottis motion has less influence on larger particles due to their dominant inertia and less sensitivity to the change of the ambient airflow field.

3.3.2. Regional deposition fractions (RDFs)

To understand the effects of the glottis motion on the regional deposition fractions (RDFs) of inhaled therapeutic particles, the transient RDFs of SG2.6 and IDG2.6 are displayed in Fig. 11. It can be observed that DFs of large particles reach the “plateau” faster than the small particles during the inhalation in the oral cavity and oropharynx (see Fig. 11 (a) and (b)). Another observation from Fig. 11 (a) and (b) is that for large particles (i.e., $d_p=10\text{ }\mu\text{m}$), the DFs in the oropharynx during the exhalation is higher in SG2.6 than IDG2.6. It is because the glottis adduction will restrain the diverging angle of the expiratory particle streams entering the oropharynx, increasing the distance between the particle and the airway walls, and thereby reducing the deposition. In contrast, the glottis adduction during the exhalation increases the chance for large particles to deposit on the airway wall of the glottis region compared to the static glottis case. Indeed, as shown in Fig. 11 (d), the DFs during the exhalation in the glottis region are 0.0177% and 0.0018% in IDG2.6 and SG2.6 ($d_p=5\text{ }\mu\text{m}$), 0.0195% and 0.0035% ($d_p=10\text{ }\mu\text{m}$). The deposition during the exhalation is substantial for particles larger than $5.0\text{ }\mu\text{m}$, which is demonstrated by the noticeable DF increases between 1.8 s and 2.2 s. The additional particle depositions during the exhalation are due to the mechanism that the

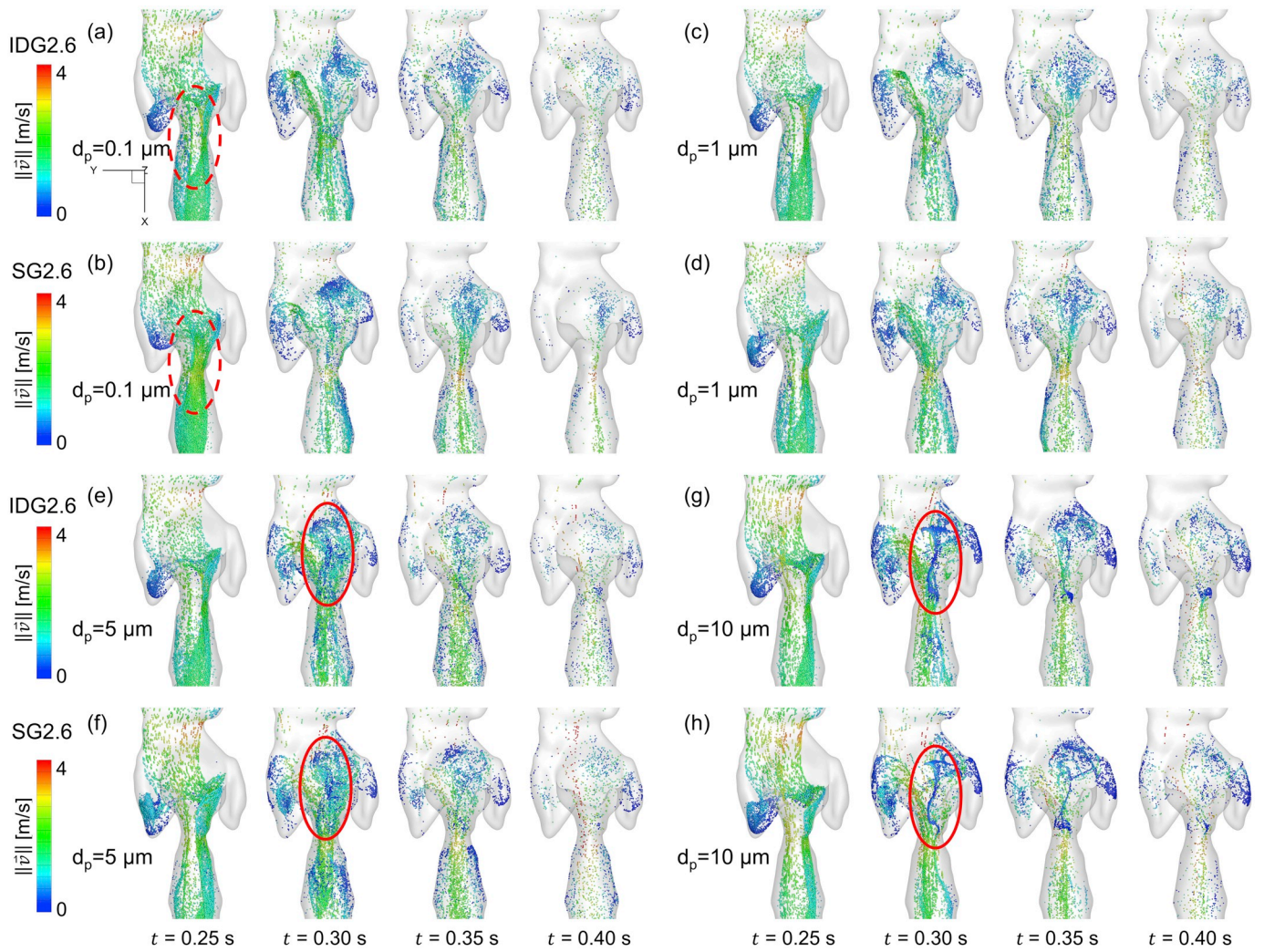


Fig. 9. Particle suspending distributions at the glottis region at $t = 0.25, 0.30, 0.35,$ and 0.40 s: (a) IDG2.6, $d_p = 0.1 \mu\text{m}$, (b) SG2.6, $d_p = 0.1 \mu\text{m}$, (c) IDG2.6, $d_p = 1 \mu\text{m}$, (d) SG2.6, $d_p = 1 \mu\text{m}$, (e) IDG2.6, $d_p = 5 \mu\text{m}$, (f) SG2.6, $d_p = 5 \mu\text{m}$, (g) IDG2.6, $d_p = 10 \mu\text{m}$ and, (h) SG2.6, $d_p = 10 \mu\text{m}$.

particles suspending near the airway wall were “waken” by the sudden change of the airflow directions from inhalation to exhalation, and obtained the extra momentum to travel and touch the airway walls.

As shown in Fig. 11 (a), with the particle size increasing from 0.1 to $10 \mu\text{m}$, the DF in the oral cavity decreases first and then increases accordingly. Specifically, the DFs of $10\text{-}\mu\text{m}$ particles for both dynamic and static glottis cases (IDG2.6 and SG2.6) are both approximately 1.8% , whereas the DFs of $5\text{-}\mu\text{m}$ particles decreases drastically to 0.4% (see Fig. 11 (a)). Additionally, the DF comparisons between IDG2.6 and SG2.6 in the oral cavity reveals that the dynamic glottis motion resulted in lower DFs except for $1\text{-}\mu\text{m}$ and $10\text{-}\mu\text{m}$ particles. Especially for $0.1\text{-}\mu\text{m}$ particles, the DF in the oral cavity at the end of the single breathing cycle of SG2.6 is almost twice as high as IDG2.6 (see Fig. 11 (a)). The reduced regional deposition in the oral cavity is due to the weakened vortices and recirculation effects in the near-wall region induced by the glottal abduction. Indeed, higher $|\overline{\omega}|$ is observed in IDG2.6 compared with SG2.6 (see Fig. 7 (b)), in which case the high $|\overline{\omega}|$ appears in the near-wall region (see Fig. 6 (d)). This indicates that the near-wall $|\overline{\omega}|$ in the oral cavity in IDG2.6 is relatively lower than SG2.6. Thus, higher $|\overline{\omega}|$ in the core region in IDG2.6 enhances momentum and energy exchanges between particles and the mainstream flows, which significantly help the particles to follow the jet core and transport downstream without deposition. Meanwhile, higher near-wall $|\overline{\omega}|$ in SG2.6 leads to higher DF

compared with IDG2.6. In the oropharynx, SG2.6 overpredicts the RDF more than IDG2.6, except for $5 \mu\text{m}$ particles (see Fig. 11 (b)). During the exhalation, a noticeable increase in deposition can be observed at $t = 1.6$ s for $5\text{-}\mu\text{m}$ and $10\text{-}\mu\text{m}$ particles in the oropharynx compared with the negligible DF increases for smaller particles. In the upper larynx (see Fig. 11 (c)), DFs are relatively higher than the other regions, especially for $10\text{-}\mu\text{m}$ particles. In the glottis region (see Fig. 11 (d)), the increasing rate of the DF in IDG2.6 is higher than SG2.6 during the exhalation after $t = 2.2$ s. As shown in Fig. 11 (e), the DFs are much lower in the lower larynx compared with other regions. An interesting finding is that the DFs for $10\text{-}\mu\text{m}$ particles are not the highest in this region. The possible reason is that most large particles have already deposited in upper regions due to the direct impaction, while the Brownian motion effect on large particles is not significant. Therefore, large particles can follow the air mainstream and travel into the trachea and avoid striking the airway wall.

The total deposition fractions (TDFs) at the end of one breathing cycle in IDG2.6 and SG2.6 are shown in Fig. 11 (f). For particle size ranges from 0.1 to $10 \mu\text{m}$, when comparing with IDG2.6, SG2.6 overpredicts the TDFs by 44.1% , 32.8% , 13.0% , 44.6% , 23.9% and 25.9% , respectively. Hence, for the mouth-to-trachea geometry employed in this study, the SG assumption could induce high prediction error (over 8%) in terms of the transport and deposition of 0.1 to $10\text{-}\mu\text{m}$ particles.

To further study whether the subject-specific glottis motion can be

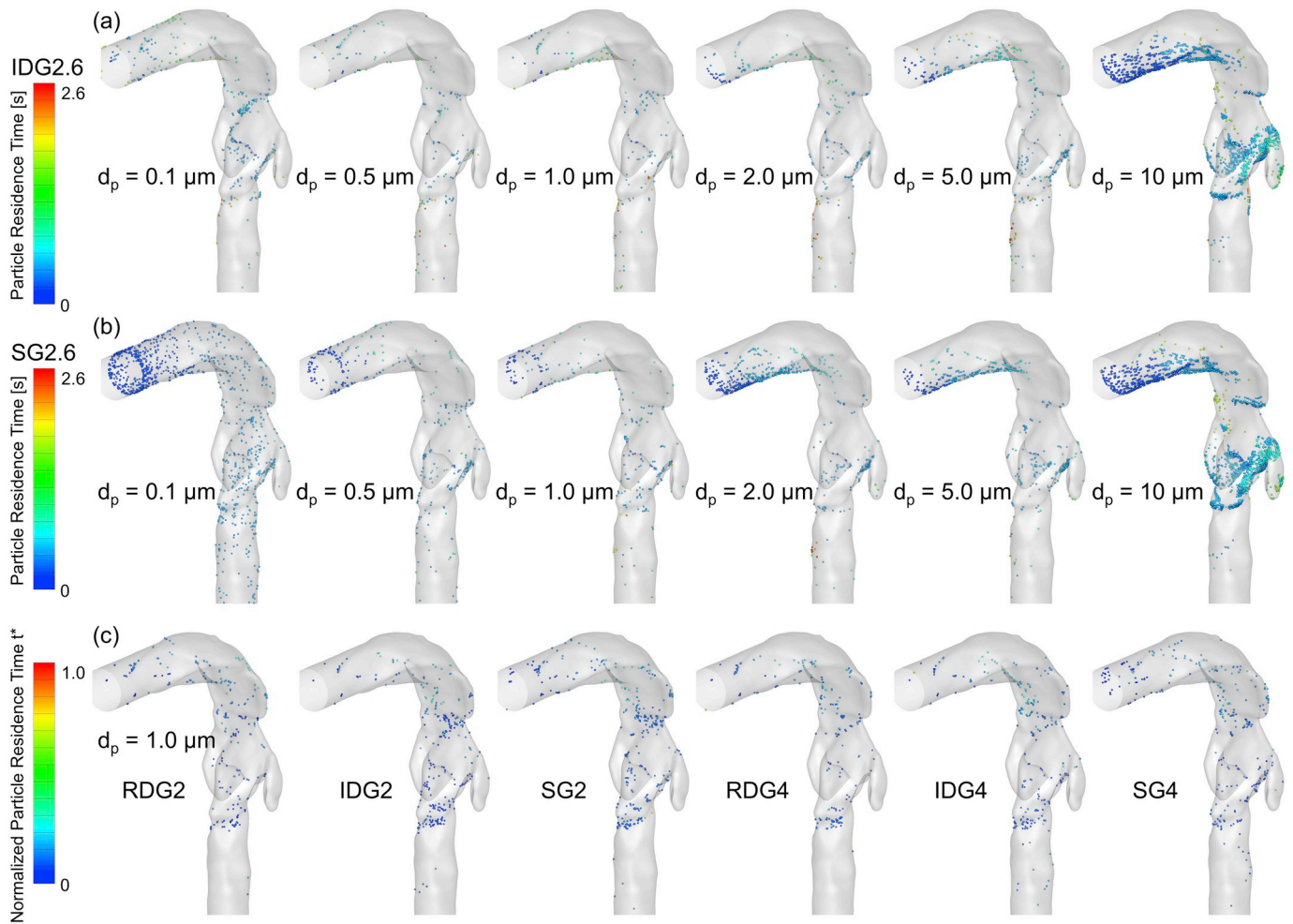


Fig. 10. Comparisons of particle deposition distributions at the end of one breathing cycle in the mouth-to-trachea geometry: (a) IDG2.6 with different particle sizes, (b) SG2.6 with different particle sizes, and (c) RDG2, IDG2, SG2, RDG4, IDG4, and SG4 for 1.0- μm particles.

simplified to idealized sinusoidal glottis motion with the same T_c and peak glottis openings, Fig. 12 (a)-(e) compare the transient DFs of 1.0- μm particles using different glottis motions associated with two distinguished breathing waveforms ($T_c = 2\text{ s}$ and $T_c = 4\text{ s}$). It can be observed that, although using the same breathing waveforms, the idealized sinusoidal glottis motion cases (i.e., IDG2 and IDG4) are not able to provide particle deposition predictions close to the subject-specific glottis motion cases (i.e., RDG2 and RDG4). Thus, in order to predict drug delivery efficiency precisely, it is necessary to obtain subject-specific glottis motion data instead of using the simplified sinusoidal glottis motions.

4. Discussion

4.1. Glottis motion effect on airflow field

The same mouth-to-trachea geometry was employed by Bernate et al. [38] numerically and Banko et al. [40] experimentally, who both investigated the airflow turbulence structures. Although similar contours of normalized velocity at the coronal plane of the vocal fold can be observed between the present study and existing papers [38,40], the clockwise vortex formed at the anterior of the glottis [38,40] is not found in this study (see the results of SG2.6 in Fig. 3). Such a difference is because the average inhalation flow rate of SG2.6 is 23.6 L/min, which is lower than other studies [38,40]. Accordingly, a lower turbulence intensity is expected with fewer noticeable vortex structures compared

with the results by Bernate et al. [38] and Banko et al. [40]. Besides, the area-averaged velocity and secondary flow intensities have also been studied in the two papers mentioned above [38,40] at multiple cross-sections similar to those shown in Fig. 4 (a). Their results indicate a similar trend of the area-averaged velocity shown in Fig. 4 (c). Furthermore, comparing the laryngeal jet and the associated recirculation at the sagittal plane between the present study (see Fig. 3) and existing numerical studies [38,41], it can be concluded that the laryngeal jet structure is sensitive to throat topology. Additionally, Fig. 4 (b) and (c) demonstrate that although the glottis abduction in IDG2.6 results in lower average velocities than SG2.6, the maximum velocity of the laryngeal jet core is higher which indicates the potentially stronger inertial impaction in the larynx and more complex secondary flows in the upper trachea.

The inter-subject variability of the glottis motion, with $d_{g,r}$ as the key feature, has a dominant effect on the airflow patterns in the mouth-to-trachea geometry. Compared with the airflow field predicted using the static glottis model, the dynamic glottis motion can either strengthen or weaken the laryngeal jet. The influence is highly dependent on the magnitudes of the glottis deformation ratio $d_{g,r}$ and the corresponding deformation rate. Indeed, Cases 3 to 5 (i.e., RDG2, IDG2, and SG2) have the lowest $d_{g,r}$ which is 1.11 (see Table 4), and the values are 1.20 and 1.40 for Cases 6 to 8 (i.e., RDG4, IDG4, and SG4) as well as Cases 1 and 2 (i.e., IDG2.6 and SG2.6), respectively. With low $d_{g,r}$, the strength of secondary flow at the vocal fold and the laryngeal jet are weakened by the glottis abduction. In comparison, when $d_{g,r}$ is 1.40, the secondary

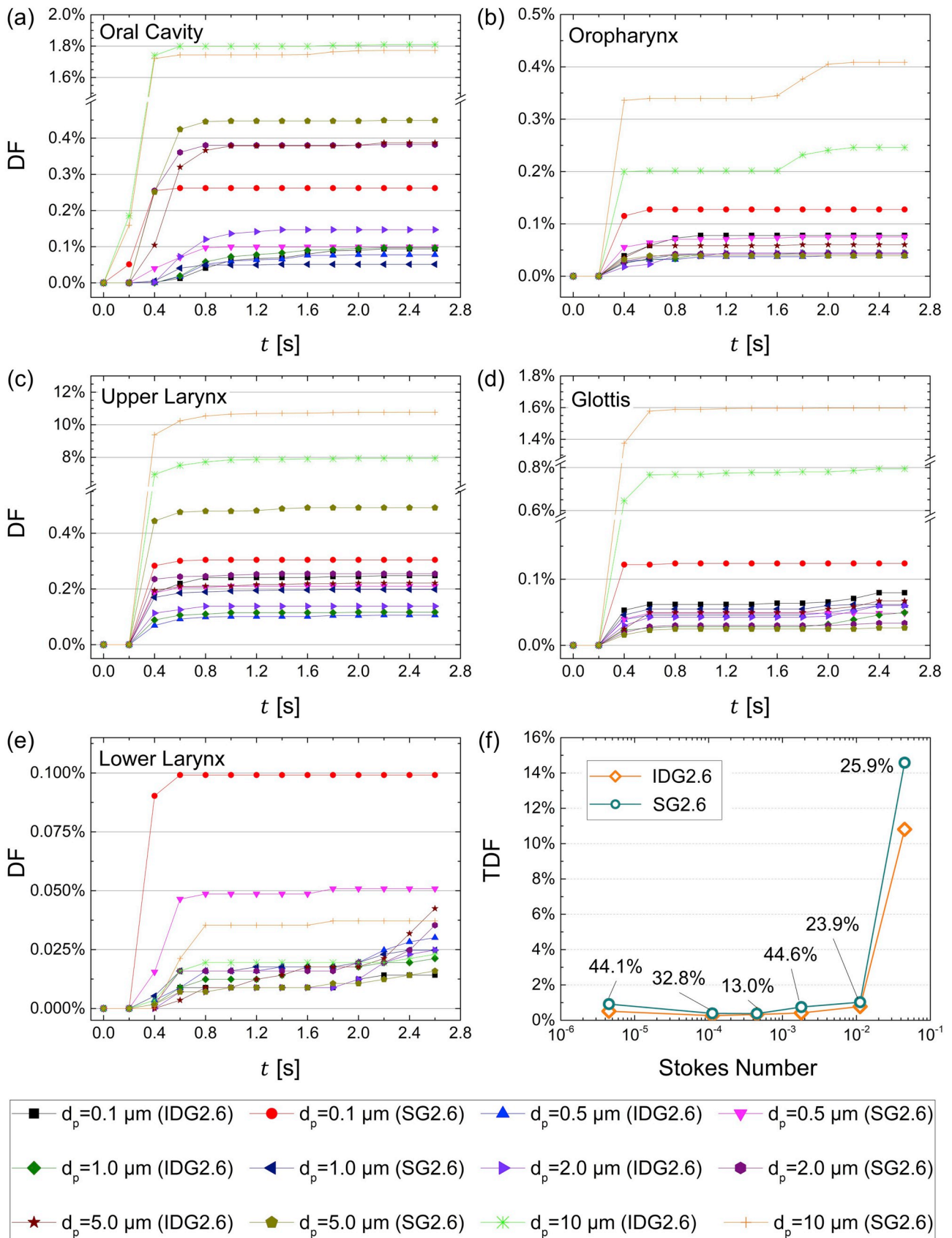


Fig. 11. Comparisons of accumulated RDFs of particles with different aerodynamic diameters between IDG2.6 and SG2.6: (a) Oral cavity, (b) Oropharynx, (c) Upper larynx, (d) Glottis, (e) Lower larynx, and (f) TDF comparisons between IDG2.6 and SG2.6 marked with relative deviation percentages.

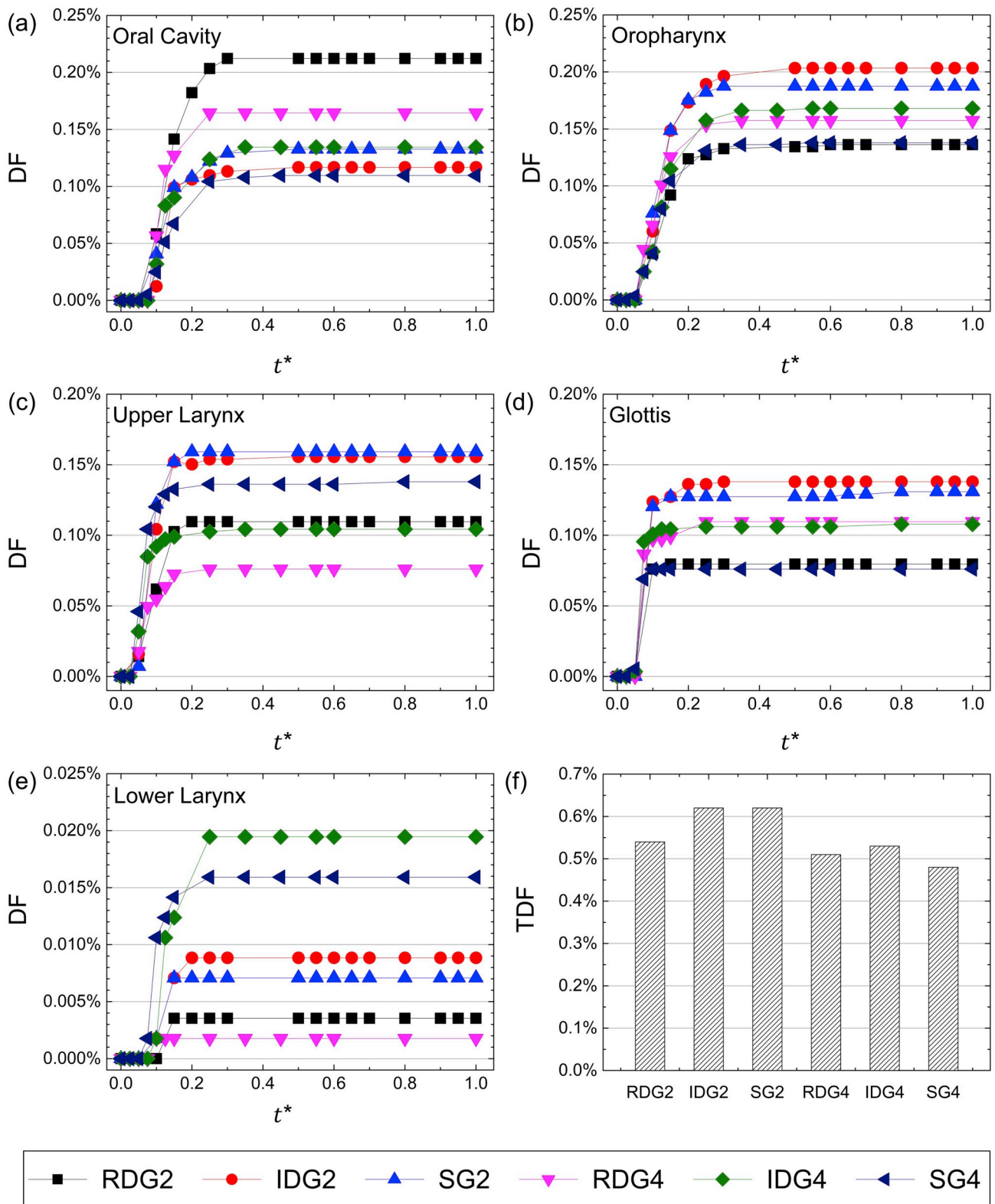


Fig. 12. Comparisons of accumulated RDFs of 1.0-μm particles with different glottis deforming models IDG2, RDG2, SG2, IDG4, RDG4, and SG4: (a) Oral cavity, (b) Oropharynx, (c) Upper larynx, (d) Glottis, (e) Lower larynx, and (f) TDFs with different glottis motions.

flow and recirculations at the vocal fold and the laryngeal jet are strengthened by the glottis abduction. Such observations demonstrate the inter-subject variabilities of the deformation ratio $d_{g,r}$ can significantly influence the local airflow pattern shifts, and must be precisely modeled based on the subject-specific clinical data.

The glottis motion also influences the pressure drop in the mouth-to-trachea geometry. The pressure drop in upper airways was experimentally investigated by Xi et al. [24], by employing physical airway models with different static glottis openings. Since the configurations of the upper airway employed in their experiment is different from the

mouth-to-trachea model employed in this study and the experimental tests were conducted with a constant flow rate, only qualitative comparisons were performed. The variation trend of the average pressure along the mainstream directions predicted by both IDG2.6 and SG2.6 models (see Fig. 4 (c)) matches their experimental results [24]. As shown in Fig. 4 (c), the pressure drops at the vocal fold at the peak inspiration flow rate are 32.7 and 31.1 Pa for IDG2.6 and SG2.6, respectively. It is interesting to notice that although the vocal fold opens wider in IDG2.6 than SG2.6, which means less minor head losses through the glottis region, the pressure drop in IDG2.6 is still higher than SG2.6. It is due to the higher momentum and energy dissipation effects induced by the higher secondary flow generated by the glottis expansion during the inhalation.

For the turbulence intensity (TI), Feng et al. [13] quantified the averaged TI at different cross-sections in seven upper airway geometries, including the mouth-to-trachea model used in this study. Relatively lower TIs were observed at the cross-sections upstream to the glottis. TI starts to increase with the airflow passes the vocal fold and reaches the maximum at the mid trachea. In this study, The TKE profiles shown in Fig. 7 (b) and (d) have similar trends. The glottis motion effect on \overline{TKE} visualized in Fig. 7 (c) is opposite to Fig. 7 (a). Although IDG and SG predict the similar trend of \overline{TKE} profiles in Fig. 7 (c), the difference in \overline{TKE} between IDG2.6 and SG2.6 is significant during the inhalation as shown in Fig. 7 (a). The possible reason is that the deformation ratio $d_{g,r}$ and its time derivative, i.e., deformation rate, for the dynamic glottis models shown in Fig. 2 (b) and (c) are smaller than the dynamic glottis model used for Fig. 2 (a) (see Table 4). As a result, the dynamic glottis models shown in Fig. 2 (b) and (c) generate minor fluctuation velocity and secondary flow during the glottis abduction, which leads to lower \overline{TKE} in DG cases than SG cases. In addition, Fig. 7 (c) indicates that during the exhalation, different glottis motions have insignificant effects on \overline{TKE} at the vocal fold. For example, despite the apparent differences of glottis deformations between RDG4 and IDG4 shown in Fig. 4 (c), \overline{TKE} values at the vocal fold during the exhalation are approximately zeros for both cases, which means that the glottis adduction may not generate high turbulent fluctuations. Such observations indicate that subject-specific glottis motion data need to be acquired in order to accurately capture the pulmonary airflow dynamics in the glottis region, instead of using the simplified static glottis or idealized sinusoidal dynamic glottis models.

4.2. Glottis motion effect on particle transport and deposition

Particle transport and deposition in the mouth-to-trachea region are influenced by multiple factors, such as the particle size, the breathing pattern, and the airway morphology. The particle size influences on the RDFs in lung airways have been well studied with the static glottis assumption [6,8,41–46]. In detail, Koullapis et al. [41] numerically investigated the particle depositions in three different airway geometries. For particles with aerodynamic diameters from 0.5 to 10 μm , their results indicate that the DF increases with the particle size increases. For steady-state inhalation with the flow rate equal to 30 L/min, the DF of 10- μm particles ranges from 15% to 82%, which is significantly influenced by the mouth-to-trachea airway morphology. Other numerical and experimental data indicate similar deposition trends for particles larger than 0.97 μm [44,45]. In this study, the DFs of 10- μm particles are 14.6% and 10.8% for IDG2.6 and SG2.6, respectively. Compared with the deposition data in the previous publication [41], the differences in TDFs are because of the different airway geometries, breathing waveforms, and the glottis motion. Instead of the monotonically increasing trend between DF and d_p , an U-curve relationship can be observed in Fig. 11 (f), which is consistent with other publications [8,46]. Specifically, Feng et al. [8] examined the DF in the upper airway model for particles from 50 nm to 5 μm and predicted higher DF for 50-nm particles than 500-nm particles in the mouth-to-trachea region. The

numerical study by Longest et al. [46] also shows DF decreases when particle aerodynamic diameter increases from 1 nm to 100 nm in a mouth-to-trachea model. Based on the numerical results in this study, the glottis motion has a significant effect on the DF predictions but has a negligible influence on the trend of DF vs. d_p . For IDG2.6 and SG2.6, the TDFs also show a U-curve trend versus the particle aerodynamic diameter (see Fig. 11 (f)). The DFs at the end of the single breathing cycle demonstrate that the static glottis assumption in SG2.6 overpredicted the particle depositions than IDG 2.6 which is more physiologically realistic. However, the influence of the static glottis assumption is complex and subject-specific. Specifically, the Particle TDF is also influenced by the deformation ratio $d_{g,r}$ of the glottis motion. As shown in Fig. 11 (f), the relative difference in TDF between IDG2.6 and SG2.6 for 1- μm particles is 13.0%. As shown in Fig. 12 (f), the maximum differences in TDFs are 12.9% among Cases 3 to 5 ($d_{g,r}=1.2$) and approximately 9% among Cases 6 to 8 ($d_{g,r}=1.11$). Thus, it can be concluded that a larger deformation ratio leads to a higher difference in TDF predictions between using DG and SG models. Furthermore, both overpredicting and underpredicting effects were discovered when using the static glottis assumption with relative differences larger than 9% (see Fig. 11 (f) and 12 (f)). Hence, the static glottis assumption has a significant influence on the TDF prediction from the oral cavity to the trachea, but the influence is subject-specific and complex. The static glottis assumption is not accurate when predicting the delivery efficiency of inhaled therapeutic particles, especially for the glottis motions with high $d_{g,r}$. To accurately evaluate pulmonary drug delivery efficiency to diseased lung sites, employing the dynamic glottis models is necessary for the accurate prediction of particle depositions in the mouth-to-trachea geometry and the resultant deposition in the tracheobronchial trees. More clinically measured glottis motions still need to be employed to study the inter-subject variability effects of the glottis motion on the deposition patterns of particles with various aerodynamic diameters.

5. Conclusions

A clinically optimized and validated dynamic glottis CFPD model has been developed and employed to simulate inhaled particle transport and deposition in a subject-specific mouth-to-trachea geometry. A generalized glottis motion function (GGMF) defining different types of glottis motions has been explicitly proposed and validated. Numerical results demonstrate the importance of recovering the subject-specific glottis motions to precisely predict the characteristics of pulmonary airflow and particle dynamics. Major conclusions are as follows:

- With the high deformation ratio $d_{g,r}$, the glottis abduction during the inhalation enhances the strength of laryngeal jet and vortices in the mouth-to-trachea region, and the adduction during the exhalation generates stronger expiratory jet flow at the vocal fold and epiglottis, which were not able to be captured using the static glottis model. With the low deformation ratio $d_{g,r}$, the glottis abduction weakens the recirculation and vortices in the larynx and glottis regions, and the glottis adduction during the exhalation results in mild expiratory jet flow compared with the static glottis model.
- The glottis motion effect on the turbulence is complex and dependent on the maximum deformation ratio $d_{g,r}$. High deformation ratio $d_{g,r}$ of dynamic glottis can increase the area-averaged turbulent kinetic energy (TKE) at the vocal fold, whereas with low deformation ratio $d_{g,r}$, the attenuation effect of glottis expansion dominates. Further investigations on the relationship between the deformation ratio and the turbulence intensity near the vocal fold with more different types of subject-specific glottis motions are required.
- Compared with the particle deposition data obtained using the dynamic glottis (DG) model, the static glottis (SG) assumption may introduce significant errors. The static glottis (SG) assumption in the

CFPD model can significantly deviate the total deposition fraction predictions for the particles with aerodynamic diameters from 0.1 to 10 μm in the mouth-to-trachea region.

- Since employing the idealized sinusoidal glottis motions is not able to accurately predict the regional particle depositions, the subject-specific glottis motion needs to be incorporated into the CFPD modeling framework.

6. Limitations and future work

Compared with the existing static glottis models, the generalized moving glottis CFPD model is more advanced and enables the *in silico* studies to characterize the subject variabilities of glottis motions on inhaled particle transport dynamics. However, there are some limitations of this study listed as follows, which will be addressed in future work.

- The RANS model, i.e., the Transition SST model, was employed instead of the more realistic Large Eddy Simulation (LES) method.
- The tracheobronchial tree and elastic lung deformation were not incorporated in the CFPD model employed in this study, and only one mouth-to-trachea geometry was employed in this study without considering inter-subject variabilities.
- Only glottis motions associated with the normal breathing conditions were simulated and investigated. The glottis motions of coughing and sneezing events, which may have full closure of the vocal fold, were not considered in this study.
- The cilia-driven mucus movement was not modeled explicitly in this study.

The future study will integrate the Discrete Element Method (DEM), Volume of Fluids (VOF), and Fluid-Structure Interactions (FSI) to develop an experimentally validated elastic whole-lung model and characterize the fluid dynamics and transport phenomena in the representative healthy and diseased human respiratory configurations. The next-generation virtual lung model will provide a more physiologically realistic *in silico* tool to optimize the personalized plan of site-specific pulmonary targeted drug delivery [13] with glottis motion and lung airway deformations.

Declaration of competing interest

The authors declare that they have no known competing financial interests or personal relationships that could have appeared to influence the work reported in this paper.

Acknowledgments

The use of ANSYS software (Canonsburg, PA) as part of the ANSYS-OSU academic partnership agreement is gratefully acknowledged (Dr. Thierry Marchal, Global Industry Director). Mr. Jianan Zhao was supported in part by appointment to the Research Participation Program at the Center for Drug Evaluation and Research administered by the Oak Ridge Institute for Science and Education through an interagency agreement between the U.S. Department of Energy and the U.S. Food and Drug Administration. The authors would like to thank Mrs. Pam Reynolds for constructive criticism of the manuscript.

References

- [1] M. Heron, National Vital Statistics Reports. National Center for Health Statistics, 2007.
- [2] J.B. Soriano, et al., Global, regional, and national deaths, prevalence, disability-adjusted life years, and years lived with disability for chronic obstructive pulmonary disease and asthma, 1990–2015: a Systematic Analysis for the Global Burden of Disease Study 2015, *The Lancet Respir. Med.* 5 (9) (2017) 691–706, [https://doi.org/10.1016/S2213-2600\(17\)30293-X](https://doi.org/10.1016/S2213-2600(17)30293-X).
- [3] V.S. Kulkarni, *Handbook of Non-invasive Drug Delivery Systems: Science and Technology*, Elsevier, 2009.
- [4] Y.S. Cheng, Mechanisms of pharmaceutical aerosol deposition in the respiratory tract, *AAPS PharmSciTech* 15 (3) (2014) 630–640, <https://doi.org/10.1208/s12249-014-0092-0>.
- [5] M. Yousefi, et al., CFD simulation of aerosol delivery to a human lung via surface acoustic wave nebulization, *Biomechanics Model. Mechanobiol.* 16 (6) (2017) 1–16, <https://doi.org/10.1007/s10237-017-0936-0>.
- [6] B. Karl, L.P. Worth, Development of an infant complete-airway in vitro model for evaluating aerosol deposition, *Med. Eng. Phys.* 58 (2018) 47–55, <https://doi.org/10.1016/j.medengphy.2018.05.002>.
- [7] H. Calmet, et al., Subject-variability effects on micron particle deposition in human nasal cavities, *J. Aerosol Sci.* 115 (2018) 12–28, <https://doi.org/10.1016/j.jaerosci.2017.10.008>.
- [8] Y. Feng, X. Chen, M. Yang, An *in Silico* Investigation of a Lobe-specific Targeted Pulmonary Drug Delivery Method, 2018 (40789): p. V001T08A011.
- [9] P.W. Longest, M. Hindle, CFD simulations of enhanced condensational growth (ECG) applied to respiratory drug delivery with comparisons to in vitro data, *J. Aerosol Sci.* 41 (8) (2010) 805–820, <https://doi.org/10.1016/j.jaerosci.2010.04.006>.
- [10] R.L. Walenga, *CFD Assessment of Respiratory Drug Delivery Efficiency in Adults and Improvements Using Controlled Condensational Growth*, Dissertations & Theses, Gradworks, 2014.
- [11] Y. Feng, C. Kleinstreuer, Analysis of non-spherical particle transport in complex internal shear flows, *Phys. Fluids* 25 (9) (2013), 091904, <https://doi.org/10.1063/1.4821812>.
- [12] Y. Feng, C. Kleinstreuer, A. Rostami, et al., Computational transport, phase change and deposition analysis of inhaled multicomponent droplet–vapor mixtures in an idealized human upper lung model, *J. Aerosol Sci.* 96 (2016) 96–123, <https://doi.org/10.1016/j.jaerosci.2016.03.001>.
- [13] Y. Feng, J. Zhao, C. Kleinstreuer, J. Wang, D.H. Wu, J. Lin, et al., An *in silico* inter-subject variability study of extra-thoracic morphology effects on inhaled particle transport and deposition, *J. Aerosol Sci.* 123 (2018) 185–207, <https://doi.org/10.1016/j.jaerosci.2018.05.010>.
- [14] H. Mortazavy beni, K. Hassani, S. Khorramyemehr, *In silico* investigation of sneezing in a full real human upper airway using computational fluid dynamics method, *Comput. Methods Progr. Biomed.* 177 (2019) 203–209, <https://doi.org/10.1016/j.cmpb.2019.05.031>.
- [15] S.H. Yeom, et al., Computational analysis of airflow dynamics for predicting collapsible sites in the upper airways: machine learning approach, *J. Appl. Physiol.* 127 (4) (2019) 959–973, <https://doi.org/10.1152/jappphysiol.01033.2018>.
- [16] P. Koullapis, et al., Regional aerosol deposition in the human airways: the SimInhale benchmark case and a critical assessment of *in silico* methods, *Eur. J. Pharm. Sci.* 113 (2018) 77–94, <https://doi.org/10.1016/j.ejps.2017.09.003>.
- [17] C. Kleinstreuer, Z. Zhang, Airflow and particle transport in the human respiratory system, *Annu. Rev. Fluid Mech.* 42 (2010) 301–334, <https://doi.org/10.1146/annurev-fluid-121108-145453>.
- [18] J. Tu, K. Inthavong, G. Ahmadi, *Computational Fluid and Particle Dynamics in the Human Respiratory System*, Springer Science & Business Media, 2012.
- [19] A. Scheinherr, et al., Glottal motion and its impact on the respiratory flow, *Comput. Methods Biomech. Biomed. Eng.* 15 (sup1) (2012) 69–71, <https://doi.org/10.1080/10255842.2012.713685>.
- [20] A. Scheinherr, et al., Realistic glottal motion and airflow rate during human breathing, *Med. Eng. Phys.* 37 (9) (2015) 829–839, <https://doi.org/10.1016/j.medengphy.2015.05.014>.
- [21] T.F. Sperry, Y. Feng, Glottis opening effects on inhaled particle Deposition in human airways. AICHE Mid-America Regional Student Conference, Rolla, Missouri, USA, 2019.
- [22] M. Brouns, S. Verbanck, C. Lacor, Influence of glottic aperture on the tracheal flow, *J. Biomech.* 40 (1) (2007) 165–172, <https://doi.org/10.1016/j.jbiomech.2005.10.033>.
- [23] C. Brücker, et al., Spectral analysis of the flow in a Glottal Model, in: *Seventh International Workshop on Models and Analysis of Vocal Emissions for Biomedical Applications*, 2011.
- [24] J. Xi, X. Si, H. Dong, H. Zhong, et al., Effects of glottis motion on airflow and energy expenditure in a human upper airway model, *Eur. J. Mech. B Fluid* 72 (2018) 23–37, <https://doi.org/10.1016/j.euromechflu.2018.04.011>.
- [25] A.J. Bates, A. Schuh, K. McConnell, B.M. Williams, J.M. Lanier, M.M. Willimering, J.C. Woods, R.J. Fleck, C.L. Dumoulin, C.L. Dumoulin, R.S. Amin, et al., A novel method to generate dynamic boundary conditions for airway CFD by mapping upper airway movement with non-rigid registration of dynamic and static MRI, *Int. J. Numer. Methods Biomed. Eng.* 34 (12) (2018) 1–19, <https://doi.org/10.1002/cnm.3144>, e3144.
- [26] S.K.A. Cheng, T. Mekonnen, H. Gholizadeh, J. Raco, L. Chen, P. Tang, H.-K. Chan, Does upper airway deformation affect drug deposition? *Int. J. Pharm.* (2019) <https://doi.org/10.1016/j.ijpharm.2019.118773>. In press.
- [27] Z. Zhang, C. Kleinstreuer, S. Hyun, Size-change and deposition of conventional and composite cigarette smoke particles during inhalation in a subject-specific airway model, *J. Aerosol Sci.* 46 (2012) 34–52, <https://doi.org/10.1016/j.jaerosci.2011.12.002>.
- [28] J. Zhao, Y. Feng, S. Mao, P. Lin, Inhalation intensity effect on lung delivery efficacy of 20(R)-Ginsenoside-Rg3-Loaded micro-particles: An *In-Silico* Study Using Large Eddy Simulation (LES), in: *BMES Annual Meeting*, 2018. Atlanta, GA.
- [29] F.R. Menter, Two-equation eddy-viscosity turbulence models for engineering applications, *AIAA J.* 32 (8) (1994) 1598–1605, <https://doi.org/10.2514/3.12149>.

- [30] R.L. Menter, S. Völker, Transition modelling for general purpose CFD codes, *Flow, Turbul. Combust.* 77 (1) (2006) 277–303, <https://doi.org/10.1007/s10494-006-9047-1>.
- [31] Y. Ostrovski, et al., Targeted drug delivery to upper airways using a pulsed aerosol bolus and inhaled volume tracking method, *Flow, Turbul. Combust.* 102 (1) (2019) 73–87, <https://doi.org/10.1007/s10494-018-9927-1>.
- [32] T.M. Crowder, et al., Fundamental effects of particle morphology on lung delivery: predictions of Stokes' law and the particular relevance to dry powder inhaler formulation and development, *Pharm. Res.* 19 (3) (2002) 239–245, <https://doi.org/10.1023/A:1014426530935>.
- [33] M.R. Maxey, J.J. Riley, Equation of motion for a small rigid sphere in a nonuniform flow, *Phys. Fluids* 26 (4) (1983) 883–889, <https://doi.org/10.1063/1.864230>.
- [34] X. Chen, Y. Feng, W. Zhong, C. Kleinstreuer, et al., Numerical investigation of the interaction, transport and deposition of multicomponent droplets in a simple mouth-throat model, *J. Aerosol Sci.* 105 (2017) 108–127, <https://doi.org/10.1016/j.jaerosci.2016.12.001>.
- [35] A. Li, G. Ahmadi, Deposition of aerosols on surfaces in a turbulent channel flow, *Int. J. Eng. Sci.* 31 (3) (1993) 435–451, [https://doi.org/10.1016/0020-7225\(93\)90017-O](https://doi.org/10.1016/0020-7225(93)90017-O).
- [36] A.D. Gosman, E. Ioannides, Aspects of computer simulation of liquid-fueled combustor, [10.2514/3.62687](https://doi.org/10.2514/3.62687) PDF 7 (1983) 482–490.
- [37] P.G. Saffman, The lift on a small sphere in a slow shear flow, *J. Fluid Mech.* 22 (2) (1965) 385–400, <https://doi.org/10.1017/S0022112065000824>.
- [38] J.A. Bernate, et al., Study of the flow unsteadiness in the human airway using large eddy simulation, *Phys. Rev. Fluids* 2 (8) (2017), 083101, <https://doi.org/10.1103/PhysRevFluids.2.083101>.
- [39] H.M. Mansour, Y.-S. Rhee, X. Wu, Nanomedicine in pulmonary delivery, *Int. J. Nanomed.* 4 (2009) 299–319.
- [40] A. Banko, et al., Three-dimensional inspiratory flow in the upper and central human airways, *Exp. Fluid* 56 (2015) 1–12, <https://doi.org/10.1007/s00348-015-1966-y>, 117.
- [41] P.G. Koullapis, L. Nicolaou, S.C. Kassinos, In silico assessment of mouth-throat effects on regional deposition in the upper tracheobronchial airways, *J. Aerosol Sci.* 117 (2018) 164–188, <https://doi.org/10.1016/j.jaerosci.2017.12.001>.
- [42] P.G. Koullapis, et al., Particle deposition in a realistic geometry of the human conducting airways: effects of inlet velocity profile, inhalation flowrate and electrostatic charge, *J. Biomech.* 49 (11) (2016) 2201–2212, <https://doi.org/10.1016/j.jbiomech.2015.11.029>.
- [43] P.G. Koullapis, et al., An efficient computational fluid-particle dynamics method to predict deposition in a simplified approximation of the deep lung, *Eur. J. Pharm. Sci.* 113 (2018) 132–144, <https://doi.org/10.1016/j.ejps.2017.09.016>.
- [44] Y.-S. Cheng, Y. Zhou, B.T. Chen, Particle deposition in a cast of human oral airways, *Aerosol Sci. Technol.* 31 (4) (1999) 286–300, <https://doi.org/10.1080/027868299304165>.
- [45] J. Xi, P.W. Longest, Transport and deposition of micro-aerosols in realistic and simplified models of the oral airway, *Ann. Biomed. Eng.* 35 (4) (2007) 560–581, <https://doi.org/10.1007/s10439-006-9245-y>.
- [46] P.W. Longest, J. Xi, Effectiveness of direct Lagrangian tracking models for simulating nanoparticle deposition in the upper airways, *Aerosol Sci. Technol.* 41 (4) (2007) 380–397, <https://doi.org/10.1080/02786820701203223>.